Deep–Sea Research II 220 (2025) 105451

Contents lists available at ScienceDirect

Deep-Sea Research Part II

journal homepage: www.elsevier.com/locate/dsr2

Late Holocene and recent cold-water coral calcium carbonate production in Guilvinec Canyon, Bay of Biscay, France

Evan Edinger [a,*], Jean-François Bourillet [b], Lenaïck Menot [c], Franck Lartaud [d], Mathilde Chemel [d], Stephan Jorry [e]

[a] Geography Dept., Biology Dept. & Earth Sciences Dept., Memorial University, St. John's, NL, A1B 3X9, Canada
[b] Physical resources and sea floor ecosystems Department, IFREMER, Plouzané, 29280, France
[c] Université de Brest, IFREMER, Biologie et Ecologie des Ecosystèmes Marins Profonds, UMR 6197, Plouzané, 29280, France
[d] Sorbonne Université, CNRS, Laboratoire d'Ecogéochimie des Environnements Benthiques, LECOB, Banyuls-sur-Mer, 66650, France
[e] Geo-Ocean, Université de Brest, CNRS, IFREMER, UMR 6538, Plouzané, 29280, France

ARTICLE INFO

Handling editor: Prof. J Aristegui

Keywords:
Calcium carbonate production
Carbonate budget
Cold-water coral
Submarine canyon
Bay of Biscay

ABSTRACT

Cold-water coral reefs and communities can be locally important calcium carbonate factories in continental shelf and slope environments, including submarine canyons. Here we present short-term and long-term estimates of coral carbonate production by colonial scleractinian coral communities in the 750–850 m depth range in Guilvinec Canyon, northern Bay of Biscay. Short-term (annual-decadal) estimates were calculated using local coral skeletal biomass, estimated as a product of coral size and abundance from ROV video surveys, a locally generated species-specific regression between coral colony size and wet weight, and published daily or annual percent growth rates for *Lophelia pertusa* and *Madrepora oculata*. A long-term (century-millennial) estimate of carbonate accretion for the same reef was derived from a piston core through the same coral community.

Average live colonial scleractinian skeletal biomass in the Guilvinec Canyon coral mounds was 153.9 ± 39.4 g $CaCO_3$ m^{-2}. Applying published growth rates, the average annual gross carbonate production was 6.85 ± 1.79 g $CaCO_3$ m^{-2} y^{-1}, range 0–30.2 g $CaCO_3$ m^{-2} y^{-1}. This carbonate production rate was about one order of magnitude lower than previous estimates from the Norwegian shelf.

A 2011 piston core through the mound was analyzed by CT-scan and subsampled for coral abundance. An age model from previous ^{14}C and U/Th ages of coral fragments in the core yielded a long-term average coral carbonate accretion rate of 78 g $CaCO_3$ m^{-2} y^{-1} over the past ~2150 y, range 40.8 (core-bottom) to 148.5 g $CaCO_3$ m^{-2} y^{-1} in the upper half, about 1–2 orders of magnitude lower than previous estimates from other regions.

Low carbonate accretion rates observed in the Guilvinec Canyon mounds could be attributable to recent declines in live coral cover, indicated by low abundance of live corals in ROV surveys from this site, compared to other regions of the Northeast Atlantic.

1. Introduction

Benthic calcium carbonate production in non-tropical environments tends to be dominated by calcareous algae and a variety of invertebrates composing the brymol assemblage (James and Lukasik, 2010; Wisshak et al., 2010; Wisshak et al., 2015). Although cold-water coral reefs generally have a limited distribution and are known for their slow growth rates, their local contributions to carbonate production can be important in cold-water coral reefs and gardens, and marine animal forests in general (Titschack et al., 2016; Orejas and Jimenez, 2017; Wienberg and Titschack, 2017). The oceanographic conditions required for cold-water corals to grow, and coral mounds to accrete, vary in space and time, and these variations can be examined in the history of particular cold-water coral mounds (Wienberg and Titschack, 2017).

When considering both pelagic and benthic carbonate production, non-tropical shelves contribute a vast amount of total carbonate production, but mass balance suggests that up to 90% of the pelagic production dissolves before it can form part of the sedimentary record (Smith and MacKenzie, 2016). Thus, while cold-water coral mounds may be a small fraction of non-tropical calcium carbonate production,

* Corresponding author.
E-mail address: eedinger@mun.ca (E. Edinger).

https://doi.org/10.1016/j.dsr2.2024.105451
Received 22 May 2024; Received in revised form 2 November 2024; Accepted 22 December 2024
Available online 29 December 2024

they can be a regionally important, and locally dominant in the Holocene cold-water carbonate sedimentary record (Freiwald, 2002; Titschack et al., 2016).

1.1. Survey-based approach to carbonate production estimates

Calcium-carbonate budgets for tropical coral reefs were first thoroughly studied in the 1970's and 80's (e.g. Stearn et al., 1977; Scoffin et al., 1980). These were built around cataloguing the abundance and growth rates of the dominant coral species and other carbonate-producing flora and fauna on the reef, then subtracting carbonate loss from bioerosion, dissolution, and sediment export under fair weather and storm conditions (e.g. Hubbard et al., 1990; Edinger et al., 2000). Alternate approaches measured change in water alkalinity across a reef to measure gross community calcification (e.g. Odum and Odum, 1955).

More recent approaches developed rapid low-impact assessment approaches that did not require destructive sampling for coral growth rate, calcification, and bioerosion measurements (e.g. Perry et al., 2012). These rapid assessments have shown that Caribbean tropical coral reefs on average are hovering close to zero or negative carbonate budgets (Perry et al., 2013), while Indo-Pacific reefs show marked loss of carbonate production and transition to net reef erosion following ENSO events (Perry, 2018). In this paper, we apply similar methods to assess net carbonate production on cold-water coral mound in the Bay of Biscay. Most efforts to assess carbonate budgets on deep-sea coral reefs have focused on coring and geological approaches to measuring mound accretion through time (e.g. Titschack et al., 2015), with the exception of the coarse-scale analysis of carbonate production on the entire Norwegian shelf coral reef province (Lindberg & Mienert, 2005).

For tropical reefs, ability to accrete upward to balance subsidence or sea level rise and remain in the shallow waters with optimal growth conditions for reef corals is essential to maintaining net reef growth, due to the general decline in tropical reef coral calcification rates with increasing depth (Bosschler and Meesters, 1993; Perry et al., 2015). Export of coral rubble from tropical coral reefs during storms is important for understanding their ability to continue accretion (or not) (e.g. Hubbard, 1992).

For deep-sea coral mounds, the same requirements for ability to withstand wave impact do not apply. Rather, deep-sea coral mounds may accrete in response to the local current field, modifying their shape to best benefit from food delivery (Bøe et al., 2016; van der Kaaden et al., 2021). The matrix of deep-sea coral reefs is generally siliciclastic or mixed carbonate-siliciclastic sediment (Roberts et al., 2009; James and Lukasik, 2010). Therefore, mound growth depends on growth of the corals themselves (carbonate production) and current baffling of fine sediment (sediment accretion), resulting in mound aggradation. Either more abundant corals, or faster coral growth can thus result in greater reef growth and mound aggradation (cf. Roberts et al., 2009; Perry et al., 2012, 2013).

On the negative side of the carbonate budget, tropical coral reefs face loss of carbonate material through skeletal breakdown, mainly external and internal bioerosion (Perry et al., 2008) and sediment export, which mainly occurs during major storms (Hubbard, 1992; Scoffin, 1993; Perry et al., 2008). Deep-sea coral reef carbonate loss is potentially affected by dissolution and bioerosion, both of which are expected be accelerated by ocean acidification (Hennige et al., 2020; Wisshak et al., 2014; Schönberg et al., 2017; Büscher et al., 2022). Sediment transport in submarine canyons where many deep-sea coral reefs occur may be driven largely by turbidity currents associated with storms at continental shelf depths (Kriphounoff et al., 2014).

Increasing concentration of dissolved carbon dioxide in seawater drives ocean acidification, manifest as low calcium carbonate saturation or undersaturation (e.g. Fontela et al., 2020). While corals can still produce skeletons under conditions of aragonite undersaturation by using more metabolic energy, the dead skeletons of deep-sea corals can become brittle under undersaturated conditions (Hennige et al., 2015), a process that has been termed "coralporosis" (Hennige et al., 2020).

1.2. Bay of Biscay cold-water corals and reefs

The Bay of Biscay, known in France as the Golfe de Gascogne, hosts extensive cold-water coral mounds at upper continental slope depths, dominated by *Lophelia pertusa* (= *Desmophyllum pertusum)* and *Madrepora oculata* in waters shallower than 1000 m, and by *Solenosmilia variabilis* below 1000 m depth (van den Beld et al., 2017a,b).

The three central canyon networks extending from the Armorican continental shelf to the Bay of Biscay deep basins are most representative of the typical functioning of a submarine canyon (Bourillet et al., 2006; Toucanne et al., 2009): strong hydrodynamics due to the high (>7 m) tidal range (Kriphounoff et al., 2014), and nutrient and sediment supply from the edge of the plateau (Toucanne et al., 2009; Mengual et al., 2019).

Guilvinec Canyon is one of the approximately 100 canyons that cut into the continental slope along the northern margin of the Bay of Biscay (Fig. 1). Guilvinec canyon among is the most thoroughly documented of these canyons (Fig. 1; De Mol et al., 2011; Van Rooij et al., 2010; van den Beld et al., 2017a,b) with mini-mounds of dead corals at the top of the canyon head (van Rooij et al., 2010) and living corals developing on outcrops of hard substrates, or forming patches 10–60 m in diameter along the flank of the canyon (Bourillet et al., 2012; van den Beld et al., 2017a,b).

The combined geological and biological efforts of the BoBGeo (Bourillet, 2009; Bourillet, 2010) and BoBEco (Arnaud-Haond and Moalic, 2011) programs, consisting of multibeam sonar mapping, ground-truthing by drop camera and ROV video, biodiversity surveys and collections, and coring through several mounds provide an opportunity to examine calcium carbonate production by living cold-water scleractinian corals, and their entry into the sedimentary record within Holocene reef mounds (Arnaod-Haond & Grehan, 2011a, 2011b; Bourillet et al., 2013; Bourillet et al., 2012; van den Beld et al., 2017a,b).

Bottom temperatures in the region and depth range of Bay of Biscay coral reefs are forecast to rise by 2 °*C*, and bottom pH is forecast to decrease by 0.3 pH units by 2100 (Sweetman, 2017), implying that the Bay of Biscay may no longer host optimal conditions for any of the dominant colonial scleractinian coral species building deep-water coral mounds (Fontela et al., 2020; Morato, 2020). Furthermore, anthropogenic activities, especially bottom trawling on the Bay of Biscay continental shelf and shelf-edge, mobilize more sediments into BoB submarine canyons (Mengual et al., 2016, 2019), where most of the cold-water coral mounds occur (van den Beld et al., 2017a,b).

In this contribution, we estimate the Recent calcium carbonate production by colonial scleractinian corals on one reef mound in the Bay of Biscay, specifically in Guilvinec Canyon. This canyon was chosen because it was also the site of moorings deployed to measure currents and sediment transport (Kriphounoff et al., 2014), coral respiration chambers (Kriphounoff et al., 2014), and piston cores through the nearby coral mounds (Bourillet et al., 2013). The ensemble of measures from one site provides an opportunity to compare the ecological approach of estimating coral growth and carbonate production with the geological approach of measuring carbonate accretion in the sedimentary record (e.g. Titschack et al., 2015, 2016). First, we re-analyze Guilvinec Canyon ROV-video images to adapt a survey-based approach of estimating carbonate budgets from tropical coral reefs to the deep sea. Second, we compare these Recent estimates with coral carbonate accretion in a core through a Guilvinec Canyon reef mound, and examine the history of carbonate accretion within the core. Finally, we place the Guilvinec Canyon mound in the context of ongoing cold-water coral growth and carbonate production studies in the Bay of Biscay through the CheReef and ARDECO programs.

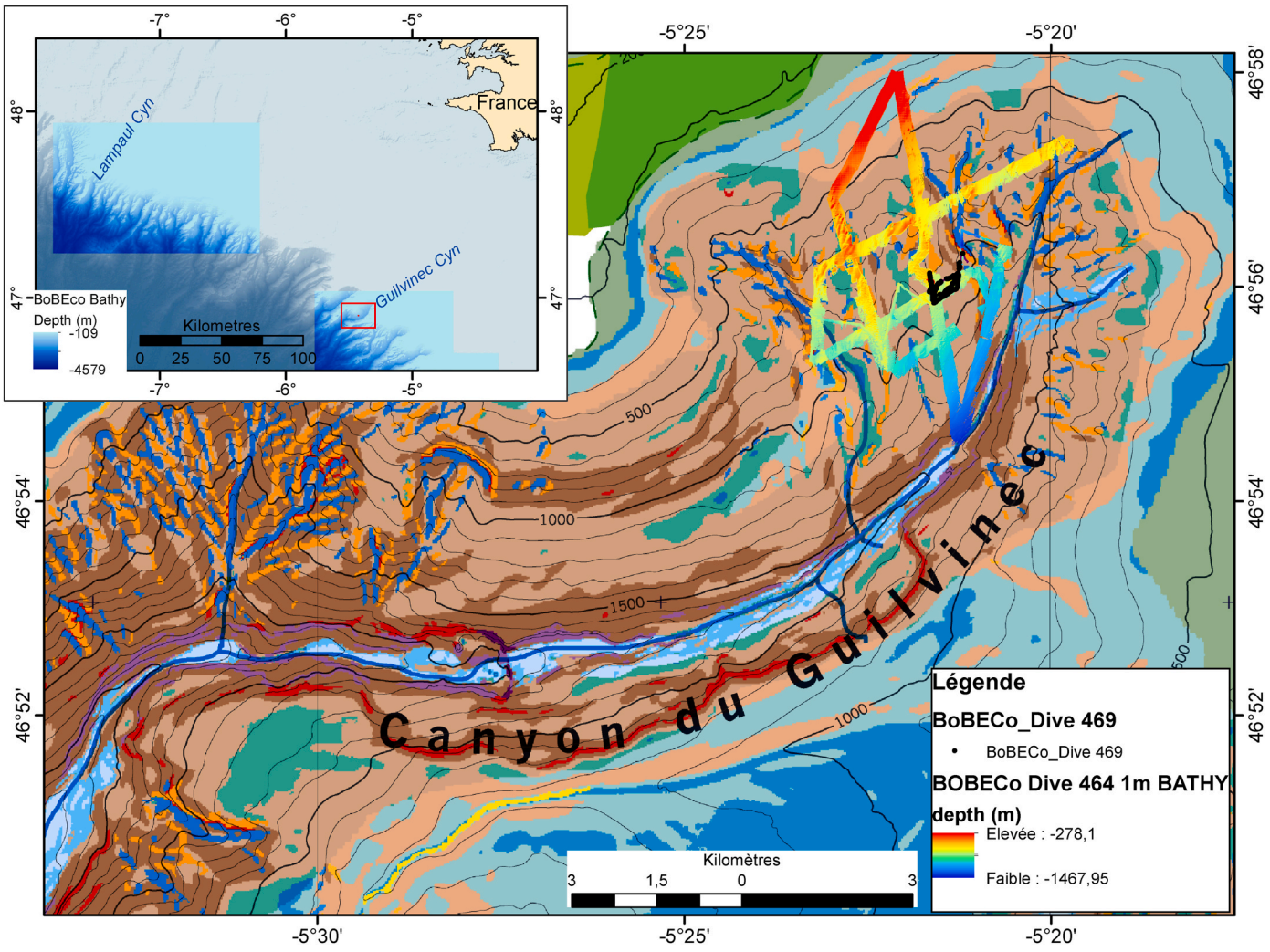

Fig. 1. Location maps. Inset:. Bathymetry of the Northern Bay of Biscay slope, showing locations of Guilvinec Canyon and Lampaul Canyon. Local bathymetry from Bourillet et al. (2012); regional bathymetry from GEBCO 2021(GEBCO compilation Group, 2021). Red rectangle indicates position of main figure. Submarine geomorphology map of Guilvinec Canyon, showing near-bottom 1m resolution bathymetry of upper Guilvinec Canyon (collected during BoBECo dive 464), and location of near-bottom video from BobEco dive 469. Submarine geomorphology Legend modified from Bourillet et al., (2012). (For interpretation of the references to colour in this figure legend, the reader is referred to the Web version of this article.)

2. Methods

2.1. Ship-based and ROV-based multibeam sonar

Ship-based multibeam sonar acquisition and analysis methods and interpreted submarine geomorphology for the study have been previously reported (Bourillet, 2009, 2010; Bourillet et al., 2102). During the BobECO cruise (2011) the ROV Victor was equipped with a near-bottom multibeam sonar unit and a low-light camera system (OTUS) (Arnaud-Haond and Grehan, 2011a, 2011b). The equipment and methods for the ROV near-bottom multibeam sonar data acquisition and OTUS low-light camera system are described in Arnaud-Haond and Grehan (2011), and in Arnaud-Haond and Moalic (2011). Processed ship-based multibeam sonar data were gridded to 25 m resolution for producing geomorphological maps (Bourillet et al., 2012). Processed ROV-based multibeam sonar data were gridded to 1 m resolution. The slope raster for the near-bottom 1m data was calculated from the bathymetric data in using the 3-D analysis tool in ArcMap 10.8. at IFREMER (Brest).

2.2. Survey-based approach to carbonate production estimates

2.2.1. ROV video image calibration and coral abundance density

Coral abundance on the Bay of Biscay cold-water coral framework communities was originally measured as percent cover of live coral, dead coral, and coral rubble, using non-overlapping video frame grabs extracted once per minute (van den Beld et al., 2017a,b). The drop cameras and ROV's used in the BobGEO and BoBEco campaigns were not equipped with underwater lasers for measuring size and distance. However, the ROV altimeter data was recorded with most of the ROV navigation data and a checkerboard photo-plate was photographed at a series of altitudes from 0.5 m to 2 m to calibrate field of view (m^2) and object sizes (cm) at varying altitudes (cf. Arnaud-Haond et al., 2017).

Using this altitude-object size calibration curve, the ROV video frame-grabs from Guilvinec Canyon used to measure coral abundance in percent cover (van den Beld et al., 2017a,b) were reanalyzed, following the method in Arnaud-Haond et al., (2017). The positions of all the Guilvinec Canyon ROV video frame-grab images were linked with the ROV navigation files in ArcGIS 10.8 (n = 532 images, acquired September 18, 2011). A total of 272 non-overlapping images were re-analyzed for the original point-count analysis, of which 197 images contained some coral (live, dead, or rubble); these are collectively

labeled as containing framework (fw > 0; van den Beld et al., 2017a,b). Unfortunately, the altimeter was turned off during some portions of the ROV dive in Guilvinec Canyon, in order to avoid interference with another instrument. After linking altimetry to non-overlapping photos, 67 images were useable for the current study.

The calculated area of field of view of all images for which altitude data were present in the navigation data was used to measure colonial scleractinian coral abundance density (N live corals m^{-2}) and to measure live coral branch length (cm) in ImageJ. Length was used, rather than length and width or outlined area (cf. Arnaud-Haond et al., 2017), as a way to adjust for parallax, knowing, however, that length might underestimate actual coral size for corals whose long axis was not orthogonal to the field of view. For images that were improperly illuminated for any reason, the field of view was adjusted to the percentage of the lateral field of view that was sufficiently bright to measure live corals, dead corals, and coral rubble, in increments of 5% measured directly on the computer monitor.

2.2.2. Coral size and estimated skeletal mass

Because coral skeletal mass growth is exponential, an estimate of coral abundance density, number of colonies per m^2, is insufficient to characterize the growth potential of cold-water corals on a given reef. Abundance (n m^{-2}) and size (cm or cm^2) gives a more complete description of coral growth potential. The size of all living coral fragments in the 67 useable images was measured using ImageJ. The maximum axis length of each live coral colony seen in all the images was measured (n = 455). The length measures were calibrated to the calculated area of each image using the image size calibration tool in ImageJ. The average length of the live coral colonies in each image was calculated separately.

To convert size to estimated mass, we calculated the linear regression between coral skeleton length and mass using all the samples of colonial scleractinians from the Bay of Biscay in the IFREMER LEP reference collection. Coral samples preserved in liquid were allowed to drip dry onto an absorbent paper towel before measurements began, while dried coral samples were simply weighed. For samples preserved in liquid, wet weight, rather than buoyant weight or dry weight, was measured, in order to avoid altering the preservation condition of the samples.

Each sample was photographed, then its length, width, and maximum stem diameter of each colony was measured with digital calipers, and the coral fragment was weighed to the nearest 0.01 g on a digital balance. The collection included 24 colonies of *Lophelia pertusa*, 18 colonies of *Madrepora oculata*, and 10 colonies of *Solenosmilia variabilis*. One subfossil coral skeleton base was not measured, because its shape and density were so different from all of the live-collected samples. The numbers of dried samples, wet-preserved dead samples without coral tissue, and wet-preserved coral samples with coral tissue are reported in Table 2. The regression relating coral fragment length to weight was calculated for each species individually, for *L. pertusa* and *M. oculata* combined, and for all three species combined.

2.2.3. Estimated living skeletal biomass of coral

The length-wet-weight regression was then applied to average length of the live portion of coral colonies in each image and the abundance density (n m^{-2}) to calculate the living skeletal biomass of corals in the image, according to.

(1) Skeletal biomass (g $CaCO_3$ m^{-2}) = average length coral (cm) x mean wet weight per coral length (g $CaCO_3$ cm^{-1}) x coral abundance density (n m^{-2}).

where average length coral refers to the length of the living portion of coral colonies as observed in the seafloor imagery.

Skeletal biomass per unit area was calculated individually for each image analyzed. The descriptive statistics for skeletal biomass and carbonate production were calculated for each image. Average length

Table 1
Reported growth rates of *Lophelia pertusa* and *Madrepora oculata* by linear extension and buoyant weight gain under unaltered conditions.

Species	Location	Method	Conditions	Linear extension rate (mm y^{-1})	Mass growth rate (% d^{-1})	reference
L. pertusa	North Sea	Repeat observation	Oil platform, elevated from bottom	26.5		Gass and Roberts (2006)
L. pertusa	Gulf of Mexico	Repeated observation	Elevated oil platforms, shipwrecks	5–30		Larcom et al. (2014)
L. pertusa	Baltic Sea	Buoyant weight	Aquarium experiments, differential feeding, 7 °C		0.04–0.05	Larsson et al. (2013)
L. pertusa	NW Mediterranean	Buoyant weight	Aquarium experiments	8.8	0.03	Orejas et al. (2011)
M. oculata	NW Mediterranean	Buoyant weight	Aquarium experiments	5.1	0.115	Orejas et al. (2011)
L. pertusa	Gulf of Mexico (same location as line 2)	Alizarin red staining	Field staining	3		Brooke and Young (2009)
L. pertusa	NW Mediterranean	Calcein staining	Field staining	8.4 ± 2.7 (W/spr) 7.3 ± 1.7 (summer)		Lartaud et al. (2014)
M. oculata	NW Mediterranean	Calcein staining	Field staining	4.1 ± 1.8 (W/spr) 5.8 ± 3.8 (summer)		Lartaud et al. (2014)
L. pertusa	NW Mediterranean	Long term observation after calcein staining	Long term	2–38	0.023	Lartaud et al. (2017) Chapron et al. (2021)
M. oculata	NW Mediterranean	Long term observation after calcein staining	Long term	0–18	0.015	Lartaud et al. (2017) Chapron et al. (2021)
L. pertusa	Norway	Buoyant weight	Aquarium experiments 12 °C, 400 ppm pCO_2, no extra feeding		0.0122	Büscher et al., 2017
L. pertusa	Norway	Buoyant weight, staining, including bioerosion	Field experiments	22.12 ± 0.86	0.0122 ± 0.0103	Büscher et al., 2019
L. pertusa	Lampaul Canyon, BoB (2021-22)	Staining, linear extension	Calcein staining, field deployment; aquarium experiments	1–4.05		Chemel (2023); Chemel et al. (2024)

Table 2
Linear Regressions predicting coral sample wet weight from coral maximum dimension length (IFREMER LEP collection). Preservation condition of samples measured was summarised as dried, wet-preserved without live coral tissue (wet, dead), or wet-preserved with live coral tissue (wet, live).

Species	N samples	Dry samples	wet, dead-collected	Wet, live-collected	coefficient	y-intercept	r^2 value
L. pertusa	23	7	11	5	9.11	−44.9	0.77
M. oculata	18	4	11	2	8.84	−43.4	0.53
S. variabilis	10	1	2	6	7.98	−31.2	0.81
L. pertusa + *M. oculata*	41	11	22	7	9.02	−44.4	0.67
All species	51	12	24	13	8.92	−42.8	0.68

values reported are the average among the 67 images analyzed, not the average of the 455 individual corals.

2.2.4. Coral extension and buoyant-weight mass growth

Growth in cold-water scleractinian corals is most often measured as linear extension, mm y^{-1} (Gass and Roberts, 2006; Brooke and Young, 2009, Lartaud et al., 2014), or as buoyant weight mass growth % mass growth per day or per year (Orejas et al., 2011; Büscher et al., 2017, 2019), which is itself a function of coral colony size (table, 1; see review in Lartaud et al., 2019). Growth studies in cold-water corals rarely separate into 3 components of extension, density, and calcification, as in tropical coral growth studies. An older and larger coral colony will accrete more calcium carbonate than a younger and smaller colony, both because it has more living polyps and because its skeletal elements are thicker. The reported buoyant weight growth rates under experimental conditions most similar to the ambient conditions in the Bay of Biscay were *Lophelia pertusa* buoyant weight mass growth rates from Büscher et al., (2017), at 12° C, under "normal" pCO_2 (400 ppm), without supplemental feeding, measured at 0.010 ± 0.004 % per day. This rate was nearly identical to the daily buoyant weight growth rate of 0.0122 ± 0.0103 % per day, or 4.45% per year reported for stained and redeployed *L. pertusa* in Norwegian shelf and fjord waters (Büscher et al., 2019).

The field experiment growth rates were applied to the standing skeletal biomass of coral carbonate measured from the Guilvinec Canyon bottom photos, to estimate gross coral carbonate production (P_g) within each image. Annual gross carbonate production was calculated as.

(2) P_g (g $CaCO_3 m^{-2}$ y^{-1}) = annual buoyant weight growth rate (% $year^{-1}$) x live coral skeletal biomass (g $CaCO_3$ m^{-2})

These estimates of total coral carbonate production are gross production only; they do not account for bioerosion, dissolution, or sediment export.

2.3. Coral mound geophysical surveying and geomorphic analysis

Cold-water coral mounds in Guilvinec Canyon, dominantly *L. pertusa*, followed by *M. oculata*, were observed by the BobGeo 1 and 2 cruises. Near-bottom multibeam sonar was collected using the ROV Victor on ROV dive BoBECO 464. The mounds were surveyed with near-bottom MBES and with a ship-based CHIRP sub-bottom profiler (Arnaud-Haond and Moalic, 2011), followed by ROV Video observations on ROV dive BobECO 469. Near-bottom multibeam sonar was processed and gridded to 1 m resolution using Caraibes software (Arnaud-Haond and Moalic, 2011).

One mound in Guilvinec Canyon was successfully cored during the BobEco cruise in 2011. Attempts to core a second mound in Guilvinec and other BoB canyons were unsuccessful, but cores from a coral mound on the Irish margin recovered up to 7 m of sediment (Stapleton et al., 2013). Several mounds were mapped with ship-based sonar and surveyed with near-bottom sonar, and CHIRP sub-bottom profiler (Bourillet et al., 2013) see supplementary material). Because the ship-based sub-bottom profiles were strongly affected by hyperbolae from the steep slopes (up to 38°, at the site of core CS01), the coring target for CS01 was interpreted using imagery from the near-bottom low-light camera OTUS (Arnaud-Haond and Grehan, 2011a; Bourillet et al., 2013). The coring target for cores CS02 and CS03 was not imaged using the OTUS system.

2.3.1. Core acquisition

Three attempts were made at coring the Guilvinec Canyon cold-water coral mounds, at sites CS01, CS02, and CS03. The objective of Cores CS01 and CSO3 was to sample a coral mound with living corals at its top, as documented using the ROV and OTUS ROV-mounted b/w camera. The objective of core CS02 was to sample the fringes of a coral mound without living corals at its top.

The IFREMER piston corer was used, with a core tube length of 3 m, and a core head mass of 3.8 MT. No pilot corer was attached to the piston corer. The IFREMER corer kinematic measurement system was used to calculate the actual depths of sediments collected by the core, before deformation induced by core penetration (Bourillet et al., 2007). Raw kinematic measurements are reported in Supplementary materials.

2.3.2. Original Core analysis – splitting, sampling, dating, age model

Cores CS01 and CS02 were analyzed following standard IFREMER coral analysis protocols. Cores were stored at 5 °C until they were x-rayed, and scanned for standard geophysical logs (resistivity, gamma ray, etc.). Core CS01 was frozen and split into working and archival halves using a circular saw, which cut some of the coral fragments, but avoided displacing them (cf. Stapleton et al., 2013). Photographs of the archival half of the core show no evidence of disrupted stratigraphy (Fig. S3). Core CS02, without abundant coral fragments in the X-rays or disuprtions in the geophysical logs, was refrigerated at 5°C, and split with a wire, as per normal IFREMER core processing methods. After splitting, cores were x-rayed again, photographed, and the working half was subsampled at 5 cm increments for grain size, aragonite content, and carbonate and major siliciclastic grain mineralogy following standard IFREMER methodology (see, for example, Jorry et al., 2020). Grain size was determined by wet-sieving sediments coarser than 63 μm, and laser granulometry for silt and clay fractions using a Coulter LS200 laser microgranulometer (IFREMER, Brest, France). Mineralogy of bulk sediment matrix subsamples, not including coarse bioclasts such as coral fragments, was determined by X-ray diffraction (XRD) (see Jorry et al., 2020). Coral subsamples were documented for depth and condition before being removed for U-series dating. Matrix sediments were subsampled for planktonic foraminifera for ^{14}C-dating.

2.3.2.1. Core re-analysis. The archival half of core CS01, and both the archival and working halves of core CS02, were scanned with a Geotek X-ray CT-scanner at 108 keV, spot size of 39 μm, a resolution of 95 pixels/cm, 1:1 mode, with 10 frames per second. These CT-scans readily identified scleractinian coral skeletal fragments from surrounding sediments (Figs. S3 and S4). The higher opacity of the coral skeletons, and the clear outlines of the coral calices, enabled identification and counting of the number of coral fragments per 5 cm increment of core length. Because fragments sometimes obscured one another, coral calices were easier to recognize and count than discrete coral fragments.

Because the core had shrunk with desiccation in storage, the percentage of the core cross-sectional volume occupied by sediment was measured visually from the 2D-CT-scan, in increments of 5%.

Visible scleractinian coral calices in each 5 cm increment of the archival half of core CS01 were counted in the CT-scans throughout the length of each core. The working half of core CS01 was re-sampled for cold-water coral skeletons, sampling all coral skeletons within four increments of 5 cm each. From these subsamples, the number and species identification of coral fragments, number of coral calices, and the mass of coral fragments per cm^3 of core was calculated.

The coral carbonate mass (M_{cc}, g $CaCO_3/cm^3$) of each 5 cm increment of core (in g/5 cm increment) was calculated as:

$$M_{cc} = [N_{cf} / (V_{ct} \text{ x } (\% \text{ PS}))] \text{ x } R_{Ncf\text{-}Mcf} \text{ x } V_{ct} \quad (3)$$

Where.

N_{cf} is the number of coral fragments visible per 5 cm increment,

V_{ct} is the volume of each 5 cm increment of the split core tube, normally 196.35 cm^3

% PS is the cross-sectional area of the desiccated split core filled by sediment, as visible in the CT-scan, and.

$R_{Ncf\text{-}Mcf}$ is the calculated regression coefficient between number of coral fragments visible in the CT scan (n calices) and the mass of coral fragments (g) in the corresponding 5 cm increment of the core. Core analyses (Figs. 6–7) are presented relative to the physical cores as recovered and re-analyzed.

A linear regression was calculated between the number of coral calices counted per cm^3 of core in the CT-scan of the archival half of the core, and the mass of coral fragments measured per cm^3 of core in the corresponding core interval of the working half of the core.

2.3.2.2. Core sediment accumulation rates and age model calculation. Ten coral fragments in core CS01 were aged using U-series dating via Thermal Ionization Mass Spectrometry (TIMS) at the University of Heidelberg, Germany. These samples included nine samples from measured depths within the core, and one from the core-catcher, following standard mechanical cleaning and TIMS measurement methods (Frank et al., 2004). In addition, pelagic foraminifera from sediment samples from both CS01 and CS02 were aged using AMS-^{14}C dating at the University of Poznan Radiocarbon laboratory, following that lab's standard protocols (Goslar et al., 2004).

The age model for core CS01 was calculated using the U-series ages on the 9 coral fragments with measured depths, and the age of the coral fragments in the core catcher reported separately. Linear regressions of at least 3 sequential ages were used, rather than instantaneous accumulation rates between individual dated coral clasts to account for 2σ error in age determination and for potential time-averaging within the reef (Edinger et al., 2007). Linear regressions relating age to core depth were calculated for the entire core above the core-catcher, and in two portions of the age model separated by an apparent inflection point, with sufficient numbers of age control points to calculate a regression on either end of an apparent inflection point. The age model for core CS02 was calculated using AMS^{14}C ages for planktonic foraminiferal samples. Radiocarbon dates were calibrated using the IntCal13 calibration,

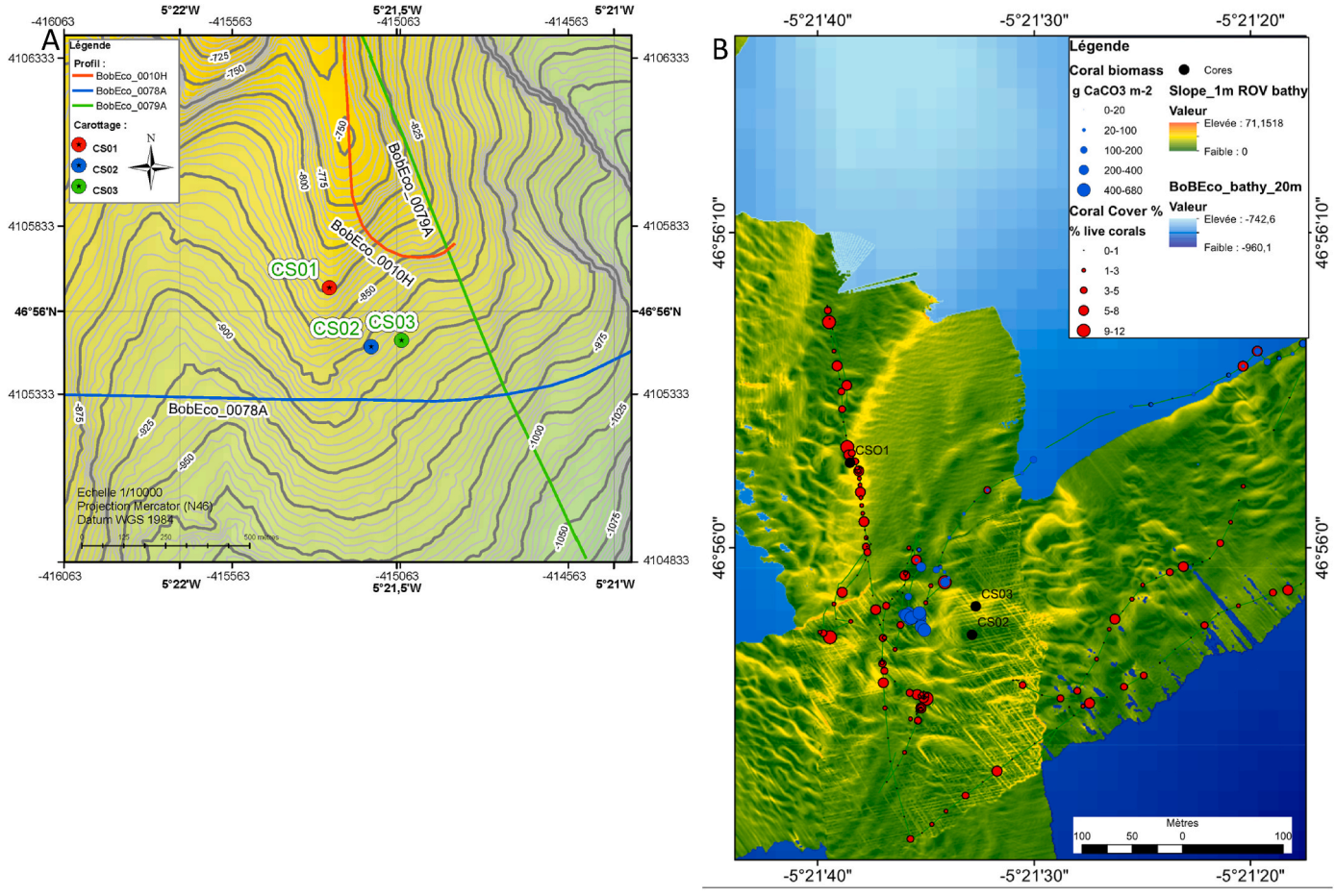

Fig. 2. A. Bathymetric contours in the portion of Guilvinec Canyon, showing location of piston coring targets and paths of 3.5 kHz sub-bottom profiles (see Fig. S1). B. High-resolution (1m) slope raster from near-bottom bathymetry collected during ROV dive 464, combined with coral skeletal biomass and % live coral cover observed during ROV dive 469, and locations of piston cores CS01 and CS02, and coring attempt CS03. Core CS01 was collected from a ridge, identified as a secondary crest in Fig. 1B. Core CS02 was collected from a flat area between two apparent sediment waves about 250 m SE of core CS01.

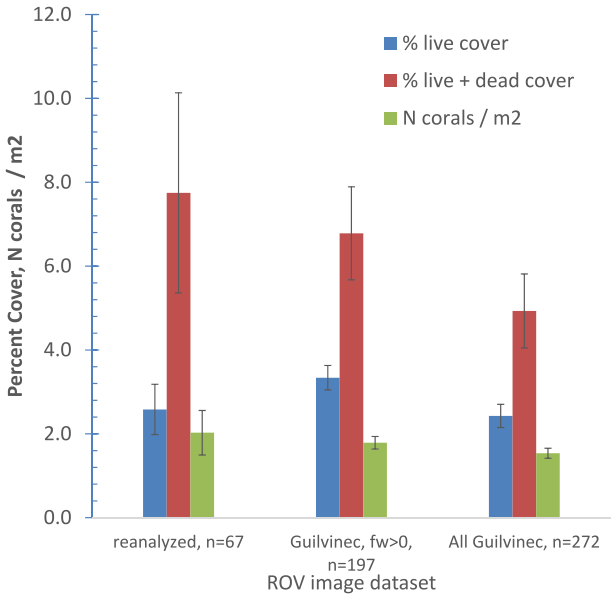

Fig. 3. Percent live coral cover, and percent cover of standing coral (live + dead) in the 67 bottom images reanalyzed for this paper, for all Guilvinec Canyon images with standing coral, and for all Guilvinec canyon images (ROV dive 469). Observed live coral density (n m^{-2}) in reanalyzed images, and calculated live coral density (n m^{-2}) in all Guilvinec Canyon images with standing coral, and for all Guilvinec Canyon images.

following the Marine13 calibration curve (Reimer, 2013).

2.3.3. Coral carbonate accretion analysis – equations & error analyses

The rate of coral calcium carbonate accretion in the core was calculated by summing the calculated coral carbonate mass of the core, extrapolated laterally to the full core diameter, over the vertical interval between each age control point from the coral U-series ages. Coral carbonate accretion rate (RA_{CaCO3}, in g coral $CaCO_3$ cm^{-2} y^{-1}) was calculated as.

$$(4)\ RA_{CaCO3} = \Sigma\ (2M_{cc}\ (\text{core interval}_{cm}))/\Delta_{\ age}\ (\text{core interval}_{cm})$$

where Σ M_{cc} is the sum of the calculated masses of coral carbonate accumulated in each 5 cm increment of a half core diameter, summed over the difference in depth between age control points, and

core interval_{cm} is the difference in depth between age control points, and

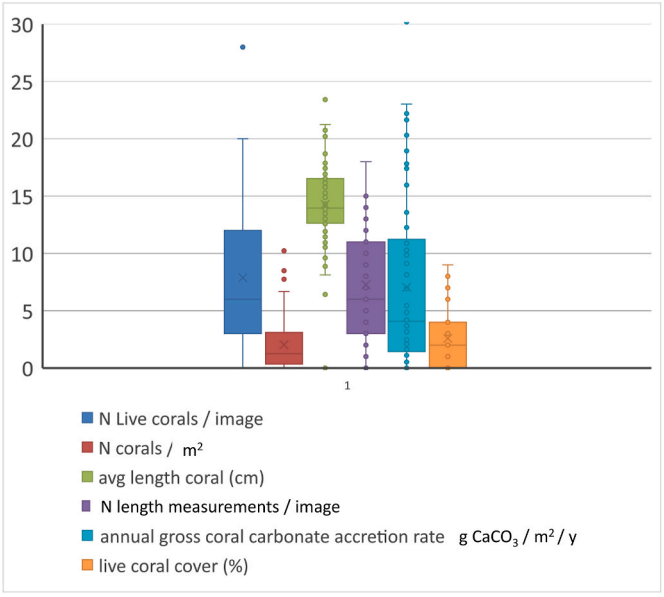

Fig. 5. Number of corals per image, number of corals per m^2, average coral length, number of length measurements per image, annual gross coral carbonate accretion rate, and percent live coral cover, in remeasured Guilvinec Canyon ROV video images (n = 67) collected during BobECO dive 469, September 2011.

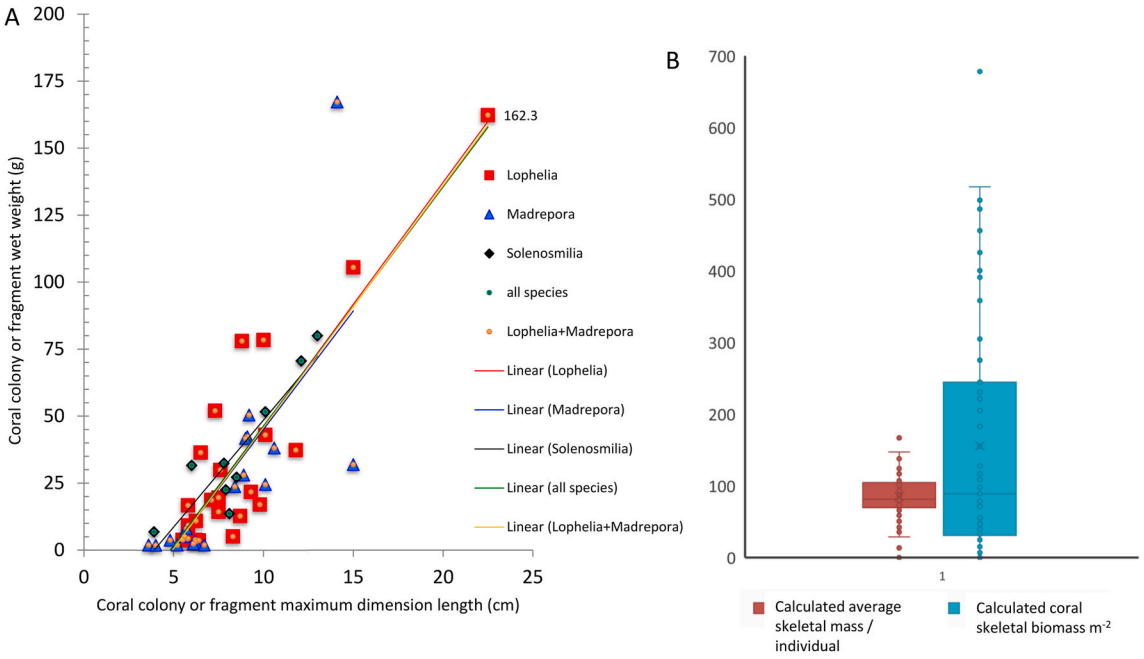

Fig. 4. A. Observed relationships between coral colony of fragment length (cm) and sample weight (g) in IFREMER Centre Bretagne LEP (BEEP) Bay of Biscay reference collection. Samples separated by species. See Supplementary Material Fig. S2 for comparison of dried vs wet-preserved samples. Regression equations and coefficients reported in Table 2. B. Calculated individual coral skeletal mass and coral skeletal biomass per m^2 in Guilvinec Canyon reanalyzed images (n = 67).

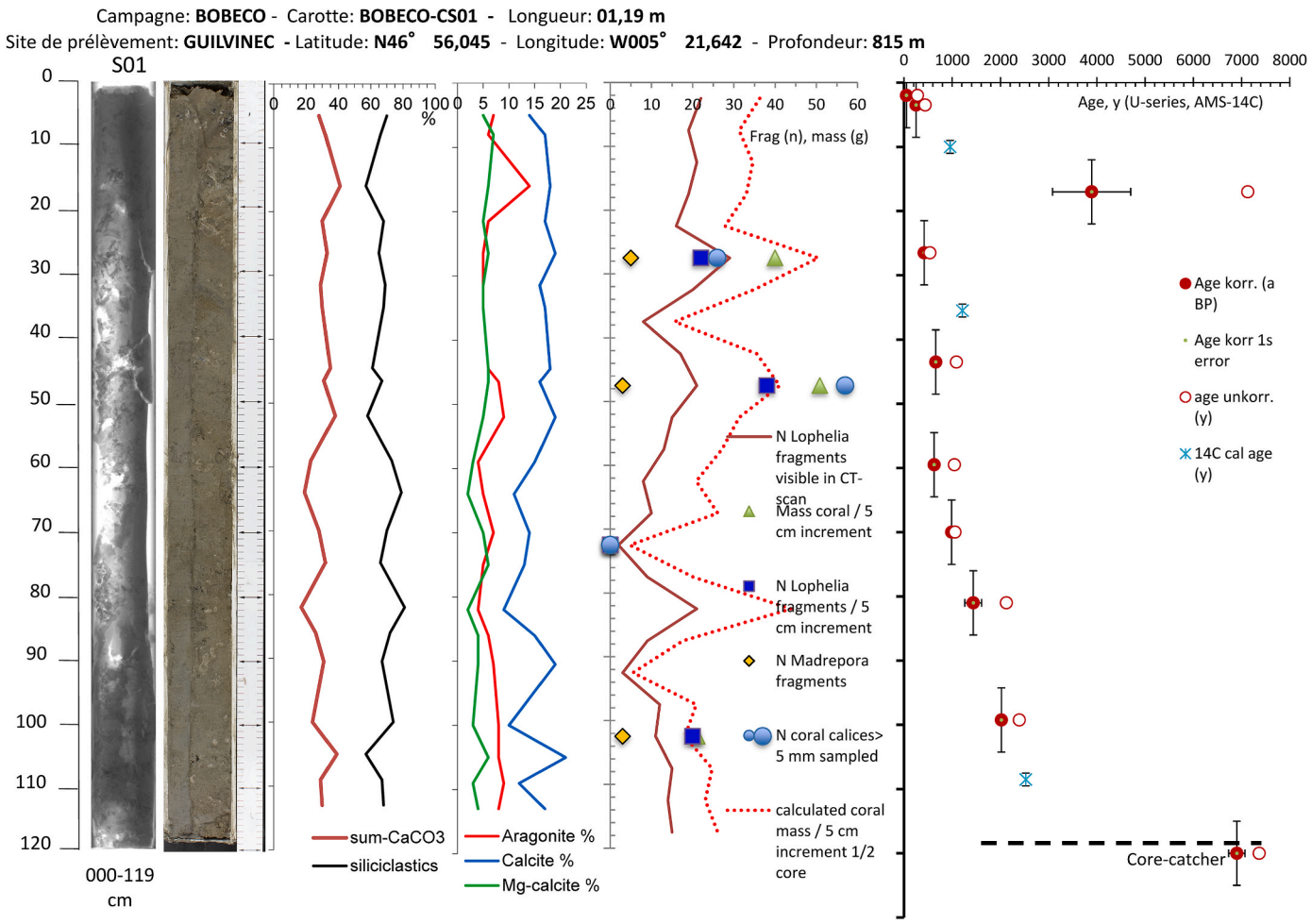

Fig. 6. Analyses of piston core BoBECO CS01. From left to right: 2-D CT-scan image of core, colour photograph of core, carbonate and siliciclastic composition of core matrix sediments, carbonate mineralogy of core matrix sediments, abundance and, subsampled mass, and calculated mass of cold-water coral fragments in core; and U-series ages of corals and AMS-14-C ages of planktonic foraminifera in matrix sediments. (For interpretation of the references to colour in this figure legend, the reader is referred to the Web version of this article.)

Δ_{age} is the difference in age between age control points derived from the coral U-series ages or planktonic foraminferan ^{14}C ages.

The corrected sediment thickness sampled by the corer (derived from the kinematic analyses, see Supplemental Material Fig. 5) was used for calculations of sediment accumulation rate and carbonate accumulation rate. To account for the 2σ error of the coral age determinations, and for time-averaging within the mound (Edinger et al., 2007), coral carbonate accumulation rates were calculated using both linear interpolation between age control points (using median values of U/Th ages), and using the average age models derived from the sediment accumulation rates derived from linear regression.

Instantaneous coral carbonate accumulation rates were calculated for each 5 cm increment of the cores, based on the interpolated ages and the linear regression-based age models, and using the corrected depths for the cores based on the kinematic analyses (Fig. S6). Average coral carbonate accumulation rates were then calculated for homogeneous segments of the cores by summing the coral carbonate accumulated within the segment, and dividing by the total elapsed time represented by each core interval. Coral carbonate accumulation rates in core were normalized to g $CaCO_3$ m^{-2} y^{-1} for comparison with the Recent observations of coral carbonate production based on the ROV surveys.

3. Results

3.1. Image useability

Of 292 ROV video frame-grab images collected in Guilvinec Canyon while the ROV was surveying, only 40% had matching altitude data in the ROV navigation records and were clear enough to use for quantitative analysis including field of view and coral abundance. A total of 67 images were suitable for re-analysis.

Average percent live coral cover in these 67 images was 2.65 ± 0.72%; while the average live coral abundance was 1.85 ± 0.55 coral colonies m^{-2} (Fig. 3).

The regression predicting total live coral abundance (N m^{-2}) from % live coral cover was calculated as.

(5) live coral colony abundance = 0.55544 live coral % cover, r^2 = 0.44, $p < 0.0001$, n = 67.

The regression predicting total live coral abundance (N m^{-2}) from % coral framework (% live + % dead) was calculated as.

(6) live coral abundance = 0.1875 (% live cover + % dead cover), r^2 = 0.60, $p < 0.0001$, n = 67.

Comparing live coral cover between the re-analyzed images (n = 67),

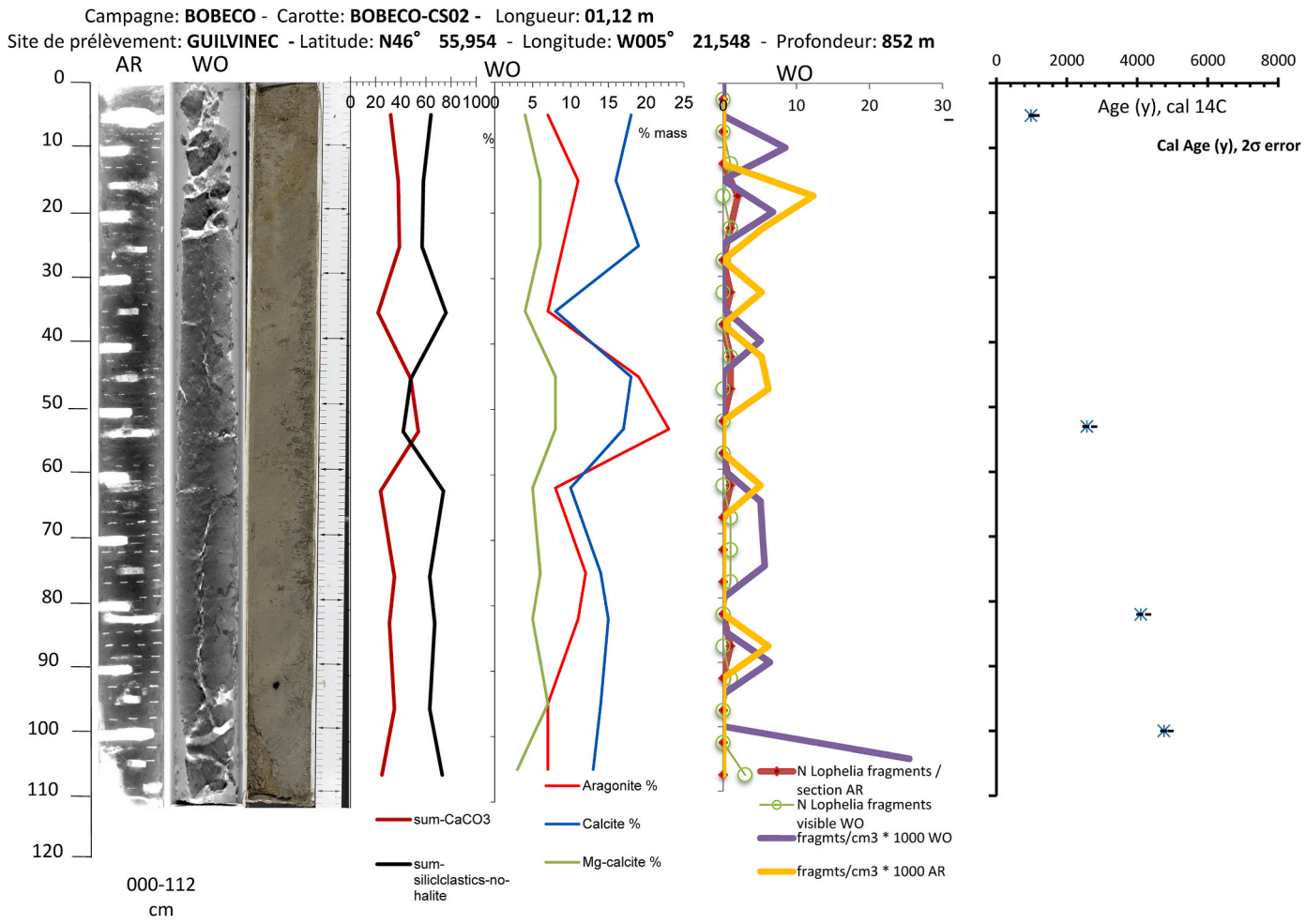

Fig. 7. Analyses of piston core BoBECO CS02. From left to right: 2-D CT-scan image of archival half of core, 2D CT-scan of working half of core, colour photograph of core, carbonate and siliciclastic composition of core matrix sediments, carbonate mineralogy of core matrix sediments, abundance of coral fragments in archival and working halves of core and calculated mass of cold-water coral fragments per cm3 of sediment in core (x1000 to improve visibility); and AMS-14-C ages of planktonic foraminifera in matrix sediments. (For interpretation of the references to colour in this figure legend, the reader is referred to the Web version of this article.)

all Guilvinec with live or dead corals (n = 197), and all Guilvinec Canyon images (n = 292) yielded similar values of % live cover and % framework (live + dead cover), and the extrapolated value of live coral abundance in the Guilvinec images beyond the 67 images re-analyzed (Fig. 3). Dead coral framework % cover in the 67 images analyzed was 5.25 ± 2.10 %, and the ratio of % dead coral cover to % live coral cover was 2.37 ± 1.29 (n = 48 images containing live corals).

3.1.1. Measurement of cold-water coral weight per size, observed average size, and calculated average living coral skeletal biomass

The average weight per length of *Lophelia pertusa*, *Madrepora oculata*, and *Solenosmilia variabilis* in the IFREMER LEP collections from the Bay of Biscay was remarkably consistent (Fig. 4a, Table 2). *Lophelia pertusa* samples included longer and heavier samples than the other two species; one subfossil *Lophelia* base was removed from the dataset because its shape and density were radically different from all other samples. *M. oculata* samples were smallest and weighed the least. *S. variabilis* samples had the strongest relationship between maximum dimension length and observed wet weight.

The resulting equation predicting coral weight from length for all species was.

(7) wet weight (g) = + 8.9 (±0.89) coral length (cm) - 42.80 (±8.01),

with an adjusted $r^2 = 0.67$, $p < 10^{-5}$, n = 50.

When calculated for *Lophelia* and *Madrepora* combined, without *Solenosmilia*, the resulting equation was.

(8) wet weight (g) = + 9.02 (±1.09) coral length (cm) - 44.44 (±9.02),

with an adjusted $r^2 = 0.66$, $F_{(1,39)} = 78.36$, $p < 10^{-10}$, n = 41.

3.1.2. Coral size, weight, skeletal biomass, and carbonate production rate

The maximum dimension length of all living coral colonies was measured in ImageJ, having calibrated the area of each image using the altimetry data. Average length values in each image were calculated separately for each image; the maximum number of coral colonies measured per image was 18, while the average value was 7.3. Of the 487 corals measured, most were determined to be *L. pertusa*, while approximately 50 were *M. oculata*, and approximately 20 could not reliably be distinguished. Overall average coral length observed was 14.5 ± 0.8 cm (average of n = 67 average length values; Fig. 5). Applying the length-weight regression for *L. pertusa* and *M. oculata* combined, the average coral skeletal biomass was calculated to be 153.9 ± 40 g/m^2 (Fig. 4b). Percent live coral cover was not a reliable predictor of coral skeletal biomass ($r^2 < 0.02$, $p > 0.17$, n = 67).

The reported experimental buoyant mass growth rate at conditions closest to the ambient conditions in the Bay of Biscay was recorded in aquaria at 12 °C, 400 ppm pCO_2, and no supplemental feeding, was

Table 3
Average coral abundance (n m^{-2}, number of corals per image, individual coral length, individual coral mass, coral skeletal biomass (g coral $CaCO_3$ m^{-2}), and average calculated gross coral carbonate production rate (g coral $CaCO_3$ m^{-2} y^{-1}), 67 images re-analyzed in Guilvinec Canyon.

	Abundance (N/m^2)	N corals/image	Coral length (cm)	Calc avg mass/coral (g)	Calc coral skeletal biomass (g coral $CaCO_3$ m^{-2}) (sum of measures)	Calc gross coral CaCO3 production (g $CaCO_3$ m^{-2} y^{-1})
mean	2.026	7.88	14.495	86.338	153.94	6.86
Std dev	2.220	6.13	3.300	29.775	168.21	7.49
N	67	67	62 images	62	67	67
95% ci	0.532	1.47	0.821	7.412	40.23	1.79
max	10.23	28	23.42	166.86	678.24	30.20
min	0	0	6.42	13.49	0.00	0.00

Table 4
Number, species composition, and mass of coral fragments recovered from core intervals, core CS01.

Depth in core (cm)	Vol Sediment/ 5 cm core Increment (cm^3)	Mass coral (g)	*L. pertusa* fragments (n)	Mass L. *pertusa* fragments (g)	*M. oculata* fragments (n)	Mass *M. oculata* fragments (g)	N calices >5 mm in corals sampled	Mass coral/ volume sediment (g cm^{-3})	N calices visible in CT scan	Vol sediment scanned (cm^3)	N calices/vol sediment CT scan (N cm^{-3})
−25	191	39.976	22	38.613	5	1.363	26	0.208	29	177	0.164
−45	191	50.834	38	50.277	3	0.557	57	0.265	21	157	0.134
−70	196	0	0		0	0	0	0	2	128	0.0157
−100	196	21.125	20	20.541	3	0.584	3	0.108	11	187	0.059

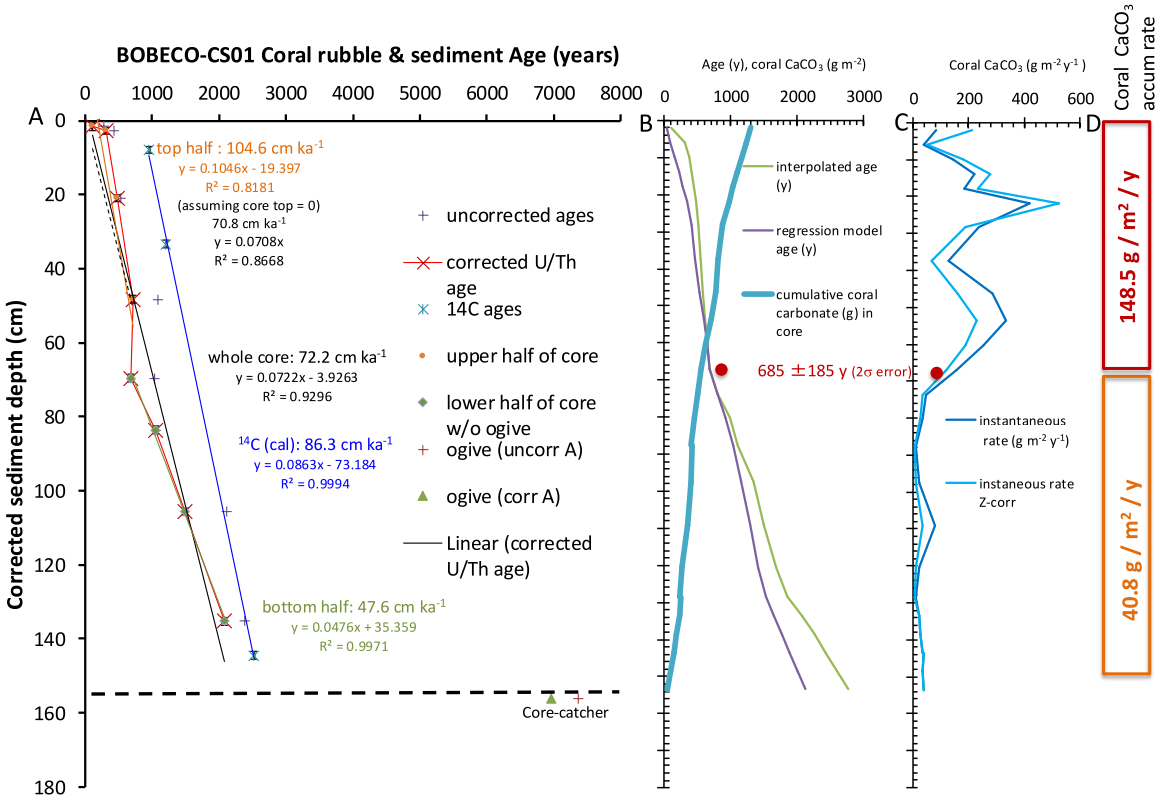

Fig. 8. Core BobECO CS01. A. Calculated age models using kinematically corrected depths of sediments. Age models for top 70 cm of sediment (top half), lower 75 cm of core (bottom half), whole core based on corals, and whole core based on planktonic foraminifera in matrix sediment; B. Interpolated and regression-based age models (treating top half and bottom half of core separately, and cumulative coral calcium carbonate in core. Red dot indicates apparent inflection point in mound accretion and carbonate accumulation. C: Instantaneous coral carbonate accumulation rate. Instantaneous rate follows interpolated age curve, while Z-corr curve follows regression-model age curve. Red dote indicates apparent inflection point in mound accretion and sediment accumulation. D. Average coral carbonate accumulation rates through bottom half and top half of core. (For interpretation of the references to colour in this figure legend, the reader is referred to the Web version of this article.)

Table 5
Uranium-series age results, cold-water coral fragments from core BobECO CS01 (courtesy N. Frank).
Measurements completed by Thermal Ionization Mass Spectrometry. ** uncorrected age based on measured data.
*** corrected age based on assumption that detritus as well as seawater contribute to total ^{230}Th activities.
Correction ratios of seawater and detritus reported in last 2 columns.
Two correction types were applied. Clean samples using high correction values based on ^{230}Th/^{232}Th of seawater estimate. Highly contaminated samples are solely corrected for detritus having much lower ^{230}Th/^{232}Th values.
Data in samples 5959, 5964, and 5962 come from very contaminated samples, and thus are unlikely to reflect true ages of the carbonate.

Lab code	Sample name	Core depth (cm)	^{238}U ±2σ (μg/g)	^{232}Th ± 2σ (ng/g)	(^{230}Th/^{232}Th)	δ^{234}U (t) (‰ ± 2σ)	(^{230}Th/^{238}U) ± 2σ	Age ** (ka ±2σ)	Age *** (ka ±2σ)	δ^{234}U (0) (‰)±2σ (abs)	Age korr. (a BP ± 1σ)	Korr. Age rel. error 2σt/t, (%)	(^{230}Th/^{232}Th corr'n)* ±2σ
IUP-5956	B.CS01-1-3	2	3.394 ± 0.003	2.320 ± 0.014	13.09 ± 1.00	140.8 ± 2.2	0.0029 ± 0.0002	0.28 ± 0.02	0.11 ± 0.08	140.8 ± 2.2	51.2 ± 44.2	81.0	8 ± 4
IUP-5957	B.CS01-2-5 cm	3.5	3.532 ± 0.004	1.857 ± 0.011	26.7 ± 2.2	143.2 ± 2.5	0.0046 ± 0.0004	0.44 ± 0.004	0.31 ± 0.08	143.3 ± 2.5	250.5 ± 37.7	24.4	8 ± 4
IUP-5959	B.CS01-16-18-degraded	17	4.134 ± 0.005	274.6 ± 2.5	3.30 ± 0.08	134.5 ± 2.4	0.0718 ± 0.0017	7.13 ± 0.17	3.95 ± 1.61	136.0 ± 7.4	3892.2 ± 811.3	41.1	1.5 ± 0.75
IUP-5960	B.CS01-26,5	26.5	3.486 ± 0.006	0.865 ± 0.015	69.3 ± 6.8	141.3 ± 3.9	0.0056 ± 0.0005	0.54 ± 0.05	0.48 ± 0.06	141.5 ± 3.9	419.2 ± 30.3	12.7	8 ± 4
IUP-5961	B.CS01-42.45	43.5	3.946 ± 0.004	5.799 ± 0.0589	23.5 ± 1.3	137.7 ± 2.1	0.0113 ± 0.0006	1.09 ± 0.06	0.72 ± 0.20	138.0 ± 2.3	660.0 ± 97.4	27.1	8 ± 4
IUP-5948	B.CS01-59,5	59.5	3.833 ± 0.0004	5.567 ± 0.045	23.1 ± 0.9	150.5 ± 3.3	0.0110 ± 0.0004	1.05 ± 0.04	0.68 ± 0.19	150.7 ± 3.4	626.6 ± 92.5	27.0	8 ± 4
IUP-5963	B.CS01-70	70	3.699 ± 0.004	0.174 ± 0.001	720 ± 22	149.0 ± 2.6	0.0111 ± 0.0003	1.06 ± 0.03	1.05 ± 0.03	149.5 ± 2.6	990.2 ± 15.8	3.0	8 ± 4
IUP-5964	B.CS01-80-81,5	81	4.485 ± 0.007	59.3 ± 1.2	5.04 ± 0.35	133.3 ± 3.0	0.0218 ± 0.0015	2.12 ± 0.14	1.49 ± 0.35	133.9 ± 3.4	1435.3 ± 173.0	23.2	1.5 ± 0.75
IUP-5962	B.CS01-98,5-100	99.25	3.737 ± 0.004	25.0 ± 0.2	11.31 ± 0.50	144.1 ± 2.4	0.0248 ± 0.0011	2.39 ± 0.10	2.08 ± 0.19	144.9 ± 2.5	2018.6 ± 94.2	9.1	1.5 ± 0.75
IUP-5958	B.CS01-ogive>8 mm	120	3.801 ± 0.006	6.248 ± 0.087	140.1 ± 5.2	154.2 ± 11.2	0.0754 ± 0.0026	7.37 ± 0.27	6.96 ± 0.34	157.2 ± 11.6	6901.8 ± 168.6	4.8	8 ± 4

0.010 ± 0.004 % d^{-1} (Büscher et al., 2017), very similar to buoyant weight mass growth rates in field conditions in Norway, 0.0122 ± 0.0103 % d^{-1} (Büscher et al., 2019). This average field-based daily mass growth rate of 0.0122 % per day, or 4.45% per year, was applied to the calculated value for living coral skeletal biomass on the Guilvinec Canyon reefs, to yield an average gross carbonate production value of 6.86 ± 1.79 g m^{-2} y^{-1} (Fig. 5; Table 3).

This gross carbonate production rate may be a slight overestimate, based upon the use of wet weight, rather than buoyant weight or dry weight of samples, particularly for *Madrepora oculata* (Table 2; Fig. S2). The length to weight regression equations for dry *L. pertusa* samples and preserved *L. pertusa* samples with coral tissue were nearly indistinguishable, while the regression coefficient for wet-preserved, dead-collected samples was 75% that of dry samples (Supplementary Information Fig. S2A). By contrast, the length to weight regression coefficients for dry *M. oculata*, wet-preserved dead-collected *M. oculata* and wet-preserved live-collected *M. oculata* varied by a factor of 5 (Supplementary Information Fig. S2B). The regression coefficients for all *L. pertusa* and all *M. oculata* samples were within 10% of each other. More than 90% of the identifiable coral colonies measured in the bottom images were *L. pertusa*.

3.2. Core analysis

Core CS01 recovered 1.19 m of sediment (Fig. 6), after an apparent penetration of 1.80 m, and a kinematic measurement of the maximum depth of the core catcher of 5.5 m below the sediment surface indicating a recovery rate of 40% (Supplementary Material Fig. S5). Core CS01 was composed of dominaintly siliciclastic sandy silt, densely packed with scleractinian coral fragments, mainly *Lophelia pertusa*, with a smaller proportion of *Madrepora oculata* in some increments of the core. The carbonate portion of the sedimentary matrix was dominated by calcite, followed by aragonite and high-Mg calcite (Fig. 6).

The maximum number of coral calices observed in the CT-scan per 5 cm increment of the archival half of core CS01 was 29, and the minimum number of calices observed was 2. The maximum number of calices per physical subsample of the working half of the core was 57, with a total weight of 50.8 g. In that subsample, 38 fragments were *L. pertusa*, 3 were *M. oculata*, and the rest were unidentified. Details of the core subsampling for coral fragments are reported in Table 4. The regression calculated between the number of coral fragments visible in the four sampled segments of CT-scan and the mass of coral fragments in each subsample was

(9) Mass coral fragments/cm^3 sediment = 1.565 * (N coral calices/cm^3 sediment in CT-scan), n = 4, r^2 = 0.95.

The calculated mass of coral skeletal fragments per volume of core averaged 27.11 ± 4.39 g per 5 cm increment, with values ranging from 5 to 50 g.

Core CS02 recovered 1.11 m of sediment (Fig. 7), with apparent penetration of 1.90 m, and a kinematic measurement of the maximum depth of the core catcher of 4.2 m, indicating a recovery rate of 37% (supplementary material, Fig. S5). CSO2 was composed of dominantly siliciclastic sandy silt, with scattered deep-sea coral fragments at a few depths within the core. The proportions of carbonate and siliciclastic minerals in the sedimentary matrix of the core CS02 was very similar to that in core CS01. The number of coral calices observed in the CTscan of core CS02 was far fewer than observed in CS01, irrespective of whether the working or archival side of the core was scanned. The maximum number of coral calices observed in a 5 cm increment from core CS02 was 3, and most 5 cm intervals had no coral calices (Fig. 8b). The maximum calculated mass of coral skeletal fragments per cm^3 of core observed in core CS02 was 2.56 × 10^{-2} g cm^{-3}, and the average was 3.105 × 10^{-2} g cm^{-3}, using the same relationship between number of coral calices observed and the mass of corals in 5 cm increments derived

Table 6
Radiocarbon results, planktonic foraminifera in matrix sediments, cores CS01 and CS02.

Core	Sample name	Lab no.	Core depth (cm)	Sample mass (mg $CaCO_3$)	Sample mass (mg C)	Age ^{14}C y BP ± 1σ	Calibrated age range (y, 2σ)	Mean calibrated age (y)	comments
CS01	BOBECO-CS01 9-11		10		0.4	1395 ± 30	880–1035	958	Planktonic foraminifera
CS01	BOBECO-CS01 35.5	Poz-56310	35.5	11.95	0.9	**1650** ± 30	1145–1281	1213	Planktonic foraminifera
CS01	BOBECO-CS01 108-109	Poz-56311	108.5	11.26	0.9	**2780** ± 30	2384–2665	2525	Planktonic foraminifera
CS02	BOBECO-CS02 5	Poz-56313	5	11.32	0.9	**1430** ± 35	908–1052	980	Planktonic foraminifera
CS02	BOBECO-CS02 53	Poz-56314	53	10.1	0.9	**2810** ± 35	2442–2689	2566	Planktonic foraminifera
CS02	BOBECO-CS02 82	Poz-56315	82	10.4	0.7	**4070** ± 35	3978–4224	4099	Planktonic foraminifera
CS02	BOBECO-CS02 100	Poz-56317	100	9.9		**4570** ± 35	4652–4857	4755	Planktonic foraminifera

from core CSO1 (equation (9)).

The percentage of carbonate and siliciclastic minerals, and the % of aragonite relative to all carbonate minerals in the fine fraction of both cores was consistent, and varied little down either core (Figs. 6 and 7). There was no relationship between the abundance of cold-water coral fragments and the percentage of aragonite in fine sediment in either cores CS01 or CS02, nor the ratio of aragonite to the sum of all carbonate minerals (linear regression, $r^2 < 0.02$, $p > 0.5$ in all cases)

3.2.1. *Radiometric dating and core age models*

The age control points for core CS01 are shown in Fig. 6, based upon 8 coral fragments and three AMS-14C dates of pelagic foraminifera in sediments. Of the coral fragments that were aged, one (at 17 cm core depth) was highly degraded, yielding a very high error term, and a date inconsistent with all the other corals in the core. Two additional dates, at depths of 81 and 99 cm, had $^{230}Th/^{238}U$ and $\delta^{234}U$ ratios departing from that of seawater, indicating possible contamination in the samples from 81 to 99 cm core depth (Table 5). Radiocarbon results are presented in Table 5, and generally indicate rates of sediment accumulation consistent with those implied from the corals, despite the evidence of apparent contamination of some coral samples.

The age control points from coral fragments in core CS01 suggested an inflection point at about 59 cm, and more rapid sediment accumulation in the upper half of the core than in the lower half, especially in the interval from 59 to 43 cm depth (Fig. 6). Therefore, mound aggradation rates in core CS01 were calculated using a linear regression of the whole core, and two additional linear regressions for the upper and lower halves of the core, separately (Fig. 8, Fig. S6). The sediment in the core catcher contained coral fragments of approximately 6902 ± 169 years, considerably older than the age of any of the other coral fragments in core CS01. The degraded coral sample from 17 cm, with clear contamination, and the coral fragments from the core catcher were not included in the aggradation rate calculations. Aggradation rates, and the regression coefficients supporting them, are reported in Table 7.

The four age control points for core CS02 from AMS-^{14}C analysis of planctonic foraminifera suggested a consistent sediment accumulation rate of 24.5 cm ky^{-1} (Table 7), with a maximum median age near the bottom of the core of 4755 years, and a 2σ age range of 4652–4857 years (Fig. 7, Fig. S6, Table 6).

3.2.2. *Sediment accumulation rates and coral carbonate sediment accumulation rates in core*

Applying the age model to the coral carbonate content in the core CS01 mound aggradation rates from the upper and lower halves of core CS01 yielded two quite different coral carbonate accumulation rates. (Fig. 8, Table 6).

The regressions and the inflection point at 59 cm depth suggest a mound aggradation rate of 47.6 cm ky^{-1} in the bottom half of the core, and an aggradation rate of 104.6 cm ky^{-1} in the upper half of the core. The average aggradation rate for the whole core was 72.2 cm ky^{-1} over approximately 2150 years based on the coral U-series ages, and 86.3 cm ky^{-1} based on the background sediment planktonic foraminifera AMS-^{14}C ages (Table 7). The foraminifera in sediment in core CS02 indicated a sediment accumulation rate of 32.4 cm ky^{-1} over approximately 4800 years (Fig. 9).

Applying the two separate sediment accumulation rates to the lower and upper portions of core CS01 yields coral carbonate accretion rates of 462 g coral $CaCO_3$ over 1443 years in the bottom half of the core, and 798 g coral $CaCO_3$ over 685 y in the upper half of the core. These carbonate accumulation rates correspond to gross coral carbonate production rates of 40.8 g coral $CaCO_3$ m^{-2} y^{-1} in the bottom half of the core, and 148.5 g coral $CaCO_3$ m^{-2} y^{-1} in the upper half of the core, when extrapolated from the 10 cm inner diameter core barrel to 1 m^2 of reef area (Fig. 8). The coral carbonate accumulation rates in core CS01 are 24–87 times higher than those in core CS02 (Figs. 8 and 9).

Table 7
Aggradation rate regressions, cores BobECO CS01, CS02. All results based on simple linear regressions, predicting age from depth. Aggradation rates in mm y-1 based on corrected core depths (accounting for kinematic deformation, see Fig. S6).

Core & interval	material	method	Depth Interval (cm)	Aggradation Rate (cm ky^{-1})	Aggradation rate (mm y^{-1})	intercept	r^2	n
CS01	coral	U-series	99–2	72.2	0.72	−3.9	0.92	8
CS01 top	coral	U-series	59–2	104.6	1.05	−19.6	0.82	5
CS01 bottom	coral	U-series	99–59	47.6	0.476	35.3	0.99	4
CS01	foraminifera	AMS-^{14}C	109–10	86.3	0.605	−73.2	0.99	3
CS02	foraminifera	AMS-^{14}C	100–5	32.4	0.324	−13.9	0.97	4

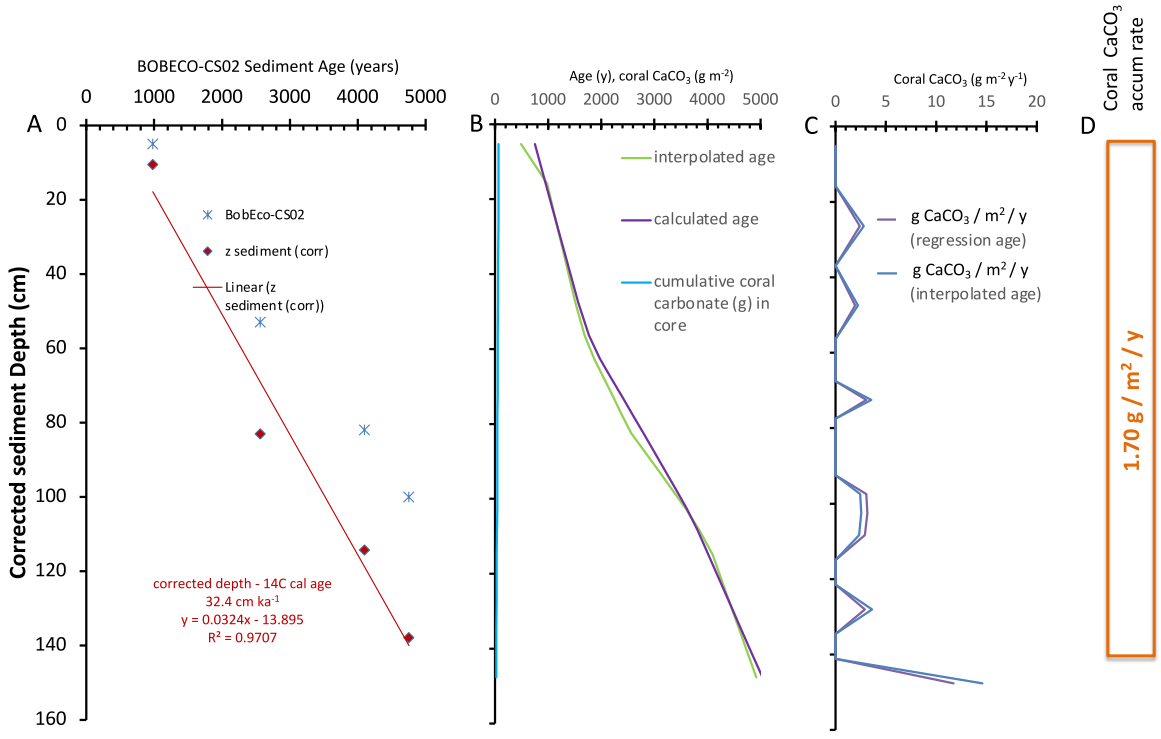

Fig. 9. Core BoBECO CS02. A. Calculated age models using corrected depths of sediments. Age models for top 70 cm of sediment (top half), lower 75 cm of core (bottom half), whole core based on corals, and whole core based on planktonic foraminifera in matrix sediment; B. Interpolated and regression-based age models (treating top half and bottom half of core separately, and cumulative coral calcium carbonate in core. Red dot indicates apparent inflection point in sediment accretion and carbonate accumulation. C: Instantaneous coral carbonate accumulation rate. Instantaneous rate follows interpolated age curve, while Z-corr curve follows regression-model age curve. D. Average coral carbonate accumulation rates through bottom half and top half of core. (For interpretation of the references to colour in this figure legend, the reader is referred to the Web version of this article.)

4. Discussion

4.1. Adaption of survey-based methodology for carbonate production to cold-water coral reefs

4.1.1. Methodology assessment

This attempt to modify survey-based approaches to carbonate budget evaluation from tropical coral reef systems to deep-water reefs yielded a simple estimate of gross carbonate production, despite considerable differences in field methods from tropical coral reefs. The coral abundance per m^2 results we report are consistent with previous reports from the Bay of Biscay (Arnaud-Haond et al., 2017), except that we were not consistently able to separate the abundance of *L. pertusa* from that of *M. oculata* in all images.

We are reasonably confident in our assessments of coral skeletal biomass. We translated coral abundance and colony size into coral skeletal biomass per unit area using a linear regression of length to wet weight, combined with the assessment of coral abundance from video. This translation was only mildly species-dependent, with the length to mass coefficient almost identical for *L. pertusa* alone and for *L. pertusa* and *M. oculata* combined. Because the regression equations for live-collected and dried *L. pertusa* fragments were nearly identical, and because the observed coral populations were >90 % dominated by *L. pertusa*, any overestimate of skeletal mass due to using wet weights of samples is likely to be less than 5%, based on the difference in regression coefficients.

In a low-diversity system like cold-water coral reefs, interspecific variation in growth rates is likely to be less important than on tropical coral reefs. Nonetheless, aquarium-based and in-situ coral growth experiments in the Mediterranean Sea have documented considerable intraspecific variation in the growth rates of the dominant deep-sea reef-building coral species (see Table 1). Only two species of corals are important contributors to calcification in the Guilvinec Canyon coral mounds, and both linear extension and buoyant weight growth rates for

both species have been quantified by us and other researchers (Gass and Roberts, 2006, Brooke and Young, 2009; Orejas et al., 2011; Lartaud et al., 2014, 2017; Büscher et al., 2017, 2019, 2022; see Table 1). Nonetheless, there is a wide variability in reported extension rates for these species in different habitats and ocean basins. Mediterranean Sea L. *pertusa* corals experienced linear extension rates of 2–38 mm y^{-1}, and 0–18 mm y^{-1} in *M. oculata*, with both inter-annual and inter-environment variation (Chapron et al., 2020).

Linear extension is more readily observed than calcification, but it is less useful for calculating carbonate production than buoyant weight gain. The buoyant weight approach is most similar to the volumetric calcification of tropical reef corals used in the ReefBudget approach (Perry et al., 2012, 2013, 2018), and is more appropriate than a simple measure of linear extension, from which mass growth would need to be extrapolated again.

Our intention had been to apply buoyant weight growth measurements from Lampaul Canyon to the measurements of coral abundance from Guilvinec Canyon. Unfortunately, the error on replicates at one time of buoyant weight measurement in *L. pertusa* and *M. oculata* from the Bay of Biscay were greater than the difference in buoyant weight recovered after four months of growth (Chemel & Lartaud, unpublished data). Higher and less variable buoyant weight growth rates for both species have been observed in Mediterranean L. *pertusa* (up to 0.023 % d-1) and *M. oculata* (0.015% d-y) (Chapron et al., 2021).

Therefore we applied the buoyant weight growth rate from the Norwegian shelf, in conditions broadly similar to the temperature and dissolved carbon dioxide values currently existing in the northern Bay of Biscay (Büscher et al., 2019). The linear extension rates observed in Norwegian waters and laboratory experiments (Büscher et al., 2017, 2019) were 1–4.05 mm y^{-1}, and similar to the 2.4 mm y^{-1} L. *pertusa* linear extension observed on in-situ growth experiments in Lampaul Canyon (Chemel, 2023). Aquarium experiments with *L. pertusa* from Lampaul Canyon yielded average extension rates of 2.2–3.5 mm y^{-1}. Corals generally grew faster in warmer water, but not always: linear extension rates were 3.5 mm y^{-1} at 15 °C, 2.6 mm y^{-1} at 10 °C, and 2.2 mm y^{-1} at 13 °C (Chemel et al., 2024).

4.1.2. *Cold-water coral reef habitats surveyed, and the condition of Bay of Biscay cold-water coral reefs*

In terms of habitat classification, the Guilvinec Canyon coral gardens and mounds best correspond to the Predominantly Dead CW Scleractinian Reef habitat (Davies, 2017). Although most Northeast Atlantic cold-water coral reefs have a large amount of dead coral and coral rubble (Davies, 2017), the live coral cover values observed in Guilvinec Canyon were quite low, with an average live cover value below 3%, and a maximum live cover of 9%. Nonetheless, live coral in Guilvinec Canyon was higher than in most of the other Bay of Biscay canyons studied (van den Beld et al., 2017a, 2017b). The maximum live coral cover observed on the Guilvinec Canyon mounds was 9%, and the maximum % live coral cover observed at any single point in the Bay of Biscay was 33%, observed on the escarpment facies (van den Beld et al., 2017a,b). Thus while the cover values seem low, the Guilvinec Canyon coral garden measured is quite typical of the coral gardens in the Bay of Biscay canyons.

Three major anthropogenic effects likely to impact Bay of Biscay coral reefs are increased sediment transport down canyons (Mengual et al., 2019), increased bottom water temperature (Sweetman, 2017), and decreasing aragonite saturation (Guinotte et al., 2006, Fontela et al., 2020; Menot et al. unpublished data). Increased sediment transport through the canyons and increased bottom water temperature may both lead to higher coral mortality (van den Beld et al., 2017a,b). Increased sediment transport has been linked to extensive shelf-edge bottom trawling in the Bay of Biscay, where fishermen have extensively reported cold-water corals and coral rubble in bycatch. (Le Danois, 1948) described extensive banks of white corals beginning in the 400–500 m depth range, before the major post-war expansion in bottom trawling. Trawling has apparently damaged and removed many of these living corals, and the trawling itself may have induced an increase in down-canyon sediment flux (Mengual et al., 2019).

A slight increase in bottom water temperatures in the Bay of Biscay and Iberian margin has been observed (Fontela et al., 2020), with a much larger increase up to 2 C predicted by 2100 (Sweetman, 2017). The forecast increases in bottom water temperature are likely to exceed the normal temperature limits of *L. pertusa*, but may favour *M. oculata* (Arnaud-Haond et al., 2017). By contrast, recent studies suggest higher resilience to temperature fluctuation in *L pertusa* than in *M. oculata* (Chapron et al., 2020).

The major piece missing from our application of the survey-based method for carbonate production is carbonate loss through dissolution, bioerosion, and sediment export (Boerboom et al., 1998; Freiwald and Wilson, 1998; Perry et al., 2012, 2014; Smith and MacKenzie, 2016; Wisshak et al., 2011, 2021). These are not quantified in the current study, but are being assessed through other ongoing experiments in the Bay of Biscay (see Menot, et al. 2023). While bioerosion *patterns* of deep-sea corals have been described extensively (Freiwald and Wilson, 1998; Boerboom et al., 1998; Beuck and Freiwald, 2005), deep-sea coral bioerosion *rates* have rarely been quantified (e.g. Wisshak et al., 2011).

Recent field experiments in Norway yielded an average bioerosion rate of -0.0020 ± 0.0015 % d^{-1}, ranging from -0.0036 ± 0.0012 % % d^{-1} on-reef to -0.0009 ± 0.0007 % d^{-1} off-reef; Büscher et al., (2019), measured using buoyant weight change. The average bioerosion rates were 16.4% of the average net coral calcification rates. The Norwegian coral bioerosion rates reported in g cm^{-2} y^{-1} are measured per unit surface area of coral colony (Büscher et al., 2019, 2022), rather than per unit area of reef, and are not directly comparable to the reef-scale coral carbonate accumulation calculated in the current study. In-vitro experimental bioerosion rates in dead *L. pertusa* coral skeletal fragments under ambient (control) conditions in aquaria were 0.006 ± 0.0013 % d^{-1} of buoyant weight, representing 8.75 ± 3.75 % of net calcification in the orange colour morph of *L. pertusa*, and 22.0 ± 9.8 % of calcification in the slower-growing white colour-morph (Büscher et al., 2022). Applying these proportions to the relative abundance of live vs dead corals in Guilvinec Canyon is not completely straight-forward, because we did not measure the abundance or skeletal biomass of dead corals per m^2. Nonethless, using the ratio of % dead cover to % live cover, the bioerosion rate per unit area of reef should be a function of the abundance of dead coral skeletons. Multiplying the ratio of bioerosion to calcification (8.75–22 % of calcification) from the two colour morphs, and scaled by the 2.37 ± 1.39 ratio of dead cover to live cover in Guilvinec Canyon, the expected bioerosion rate would be about 21–52% of the gross carbonate production rate. The coral carbonate production rate would be very low, but would still remain positive, indicating net reef growth (cf. Perry et al., 2012).

By contrast, the recent Norwegian coral calcification and bioerosion experiments demonstrated a transition to net skeletal dissolution in live corals, and combined accelerated bioerosion and abiotic skeletal dissolution, under aragonite saturation values below $\Omega_a = 0.75$ (Büscher et al., 2022). Similarly, Guilvinec Canyon reefs would transition to net reef erosion by processes that increased coral mortality, or processes that increased the rate of bioerosion (cf. Perry et al., 2013).

Ocean acidification is predicted to weaken the skeletons of aragonitic deep-sea coral reefs, through increased post-mortem dissolution or corrosion (Hennige et al., 2015, 2020). Sponge bioerosion on tropical coral reefs and temperate shelf habitats increased under experimental acidification (Wisshak et al. 2012, 2014; Schönberg et al., 2017). Bay of Biscay waters in the depth range where Guilvinec Canyon corals occur are predicted to experience a decrease in pH of 0.3 pH units (Sweetman, 2017). Combined with the forecast 2 °C increase in temperatures (Sweetman, 2017), these waters would have aragonite saturation values below $\Omega_a = 1$, by 2100 (Sweetman, 2017; Fontela et al., 2020; Menot et al., unpublished data from Lampaul Canyon). In undersaturated conditions, abiotic dissolution would likely increase for living coral

skeletons, and combined bioerosion and dissolution would dramatically increase in dead coral framework, reaching carbonate loss rates of 0.010 % d^{-1}, nearly equivalent to the net calcification rates we have applied under normal conditions (Büscher et al., 2022). Because dead framework was more abundant than live corals on the Bay of Biscay reefs (van den Beld et al., 2017a,b), as is generally the case for Northeast Atlantic cold-wter coral reefs (Roberts et al., 2009), the net result at the reef scale for Bay of Biscay reefs would likely result in net reef erosion by 2100. This transition agrees with the projected decrease in habitat suitability for *L. pertusa and M. oculata* in nearly all of the Northeast Atlantic resulting from climate change and ocean acidification (Morato, 2020).

4.2. Accumulation rate differences between surface surveys and sediment cores: effects of time-averaging?

4.2.1. Time-averaging

Time-averaging is a ubiquitous process in the sedimentary record, and relates to the relative rates of accumulation of bioclasts and their enclosing sediments (Kowalewski, 1996). Differences in carbonate accumulation rates between the surface surveys and the sediment cores may be attributable to time-averaging, despite the feedback between cold-water coral growth and cold-water coral reef aggradation (James and Lukasik, 2010; Wienberg and Titschack, 2017). Apparent coral carbonate production rates in surface surveys were 1–2 orders of magnitude lower than coral carbonate accumulation rates observed in the two piston cores. This difference is consistent with differences in abundance and diversity between living assemblages and death assemblages for a variety of bioclasts in siliciclastic settings (reviewed by Tomašových et al., 2023), and is similar to differences between living assemblages and fossil assemblages in tropical coral reefs (Edinger et al., 2001). In tropical coral reef systems, the accumulation of dead corals of fast-growing species can lead to an over-representation of those species relative to slow-growing species (Edinger et al., 2001).

Nonetheless, time-averaging on reefs includes both a spatial and temporal dimension. Corals at the same stratigraphic horizon of a tropical coral reef show considerable variation in radiocarbon age (Edinger et al., 2007). Similarly, "core-top" coral fragments in the top 5 cm of core CS01 returned U/Th ages up to 300 years. This large age range in the top 10 cm of the core could reflect disturbance of the core-top by the piston corer, or mixing of old and young coral fragments in the coral rubble at the sediment surface. This pattern is not likely to be the result of bottom trawling. Bottom trawling in the Bay of Biscay occurs widely on the continental shelf, including the degraded shelf-edge reefs, but rarely extends as deep as 800 m into the submarine canyons (Mengual et al., 2019.) Cold-water coral fragments recovered from the southeast flank of Guilvinec Canyon in a shallow box-core from about 800 m water depth had ages ranging from 1.21 to 2.27 ka (de Mol et al., 2011).

The ~7ka coral rubble recovered from the core-catcher represents a hiatus in coral growth in the precise location of our core CS01, with coral growth resuming above this surface around 2.2 ka. Causes of a potential hiatus could be local or regional and are impossible to determine from the data available for this study. Acoustic (3.5 kHz) sub-bottom profiles acquired prior to coring had strong hyperbolae reflecting uneven topography, which obscured surface sediment stratigraphy (Fig. S1). The fact that sedimentation in core CS02 continued without apparent interruption since before 4 ka suggests that the coral mound stopped or laterally shifted its aggradation, but that other sedimentary processes continued. Holocene hiatuses in cold-water coral mound growth are well-documented elsewhere in the Northeast Atlantic (e.g. Douarin et al., 2013).

4.2.2. Mound aggradation rates

In this study we calculated mound aggradation rates by linear interpolation between age control points, and by linear regression in consistent segments (cf. Edinger et al., 2007). The resulting mound aggradation rates and carbonate production rates were generally consistent between these two approaches, with the exception of the top 5 cm of CS01, which may have been disturbed by the coring process. One date in core CS01, at 43 cm depth was included in the linear regression, but excluded from the linear interpolation, because using the median age value for interpolation introduced an apparent age reversal, and a negative value of interpolated aggradation rate. The 2σ age ranges of this point and the point below it, at 59 cm depth, clearly overlapped, showing that this age control point did not represent sediment mixing, but rather, age uncertainty in a rapidly accreting mound (Table 4). These age control points, despite high age precision, indicate the value of using a multiple-value regression over individual segment interpolation for determining age models and describing sediment accumulation rates and carbonate production rates (cf. Edinger et al., 2007).

Although the rates of mound aggradation (≅ sediment accumulation) in sediment core CS01 were extremely high for the deep-sea, rivalling rates typical of some tropical coral reefs (Pandolfi, 2006; Edinger et al., 2007), similar mound aggradation rates have been observed in deep-sea coral reefs in the Mediterranean Sea and Norwegian margin (Titschack et al., 2015, 2016; Wienberg and Titschack, 2017), and similar sediment accumulation rates have been observed elsewhere in the Bay of Biscay (Penaud, 2020). The mound aggradation rate in core CS01 showed a dramatic increase at mid-core depth (~60 cm depth, about 685 years ago, from 48 to 105 cm ka^{-1}). Even core CS02, collected near a reef, but with very little coral rubble present in the core, showed rates of sediment accumulation of about 30 cm ka^{-1}.

The accumulation of dead coral skeletons can occur in the form of consolidated and possibly compressed rubble relative to the enclosing sediment (Kowalewski, 1996), even though in the case of cold-water coral reefs, the presence of the corals increases the rate of mound aggradation by baffling currents (James and Lukasik, 2010; Titschack et al., 2015; van der Kaaden et al., 2021). In a low-diversity system like deep-water coral reefs dominated by a few species of colonial scleractinians, this effect of time-averaging can emphasize faster accumulation of skeletons than ecological surveys of a living reef might suggest.

In the case of the Bay of Biscay coral reefs, time-averaging effects may be accentuated by recent degradation of Bay of Biscay cold-water corals associated with anthropogenic environmental change (see above), which may have depressed live coral cover and live coral biomass. Without longer term ecological records of coral abundance in the Bay of Biscay, it is difficult to determine the degree of this accentuation. The extensive coral banks at the shelf-edge described by (Le Danois, 1948) likely included both relict subfossil and living corals, and appear to be have been extensively damaged by bottom-contact fishing, and sediment mobilized by trawling elsewhere on the shelf (van den Beld et al., 2017a,b; Mengual et al., 2019). Nearly a century ago, French scientists warned fishermen in the Bay of Biscay about ecological damage to cold-water corals induced by fishing, especially bottom-trawling (Joubin, 1922). An alternate interpretation, that the shelf-break banks represent coral accumulation under colder early-Holocene conditions (de Mol et al., 2011) cannot be categorically rejected.

The difference between corals in U/Th ages and calibrated ^{14}C ages from their enclosing sediments was considerable, with planktonic foraminifera in the enclosing sediments suggesting ages 700–900 years older than corals at the same core depth. Nonetheless, the full-core rates of mound aggradation calculated using U-series ages from corals (72 cm ka^{-1}) or ^{14}C ages from planktonic foraminifera (86 cm ka^{-1}) were quite similar. Core-top sediment disturbance by the piston-corer could not explain the systematic offset in ages throughout the length of the core.

The relatively consistent age offset downcore suggests that the sediment-water interface lies considerably below the coral-water interface, especially in a fast-growing reef, consistent with observations of healthy reefs (Roberts et al., 2009). Corals alter near-bottom boundary layer currents and trap sediment; taller corals cause a greater reduction on near-bottom turbulence than smaller corals (Zedel and Fowler, 2009). Nonetheless, an age difference between corals and sediments of

600 years represents nearly 40 cm worth of coral mound accretion (see Fig. 9a) above the sediment-water interface, much larger than the average sizes of Recent corals observed in the underwater video data. It is possible that the average height of living corals was greater, and the distance between the top of corals and the top of sediment was greater, when reef aggradation rates were at their maximum. We note that the apparent offset between coral age and sediment age is less in the lower half of the core when aggradation rates were lower.

Another explanation could be that the coral debris are not in place. They could be older and could have been transported from upslope by gravity currents as both BOBECO-CS01 and BOBECO-CS02 are located in areas with apparent sediment waves, as illustrated in the slope map in Fig. 2B. But this hypothesis is not well supported by i) coherent sediment ages for BOBECO-CSO1 core and ii) a systematic offsets from the bottom to the top of the core except if the current is strong enough to remobilize the coral debris but not enough for the muddy sand of the area. A clearer explanation of the offset between coral U-series age and enclosing sediment ^{14}C age would require dedicated paired sampling of corals and sediments at multiple depths down-core.

4.2.3. Composition and origins of carbonate minerals in the fine fraction of cores

The enclosing sediment in the fine fraction of the cores was consistently dominated by siliciclastic silt to fine sand. All carbonates together typically summed to less than 40% of the fine sediment fraction (Figs. 6–7). This pattern is consistent with other cold-water coral reefs in the Northeast Atlantic (James and Lukasik, 2010; Titschack et al., 2015; Wienberg and Titschack, 2017). In this paper, we calculated carbonate production by corals, but not total carbonate accretion, since the origin of carbonates in the fine sediment fraction is unknown, and likely represents a mixture of hemipelagic and detrital sources (see below). Down-core analyses showed no relationship between aragonite % in the fine fraction and the abundance of cold-water corals in either core, and the mineral composition of the carbonates in the fine fraction of sediments was consistent between the two cores. The lack of a relationship between coral abundance and aragonite in the fine sediments implies that the carbonate fraction of the fine sediment matrix is independently derived from coarse-grained coral carbonates. This apparent scarcity of aragonite from *in-situ* corals, also implies that sponge bioerosion to produce silt-sized fragments of coral-derived aragonite (Wisshak et al., 2014) proceeded very slowly relative to the rate of burial.

The most likely sources of carbonate minerals in the fine fraction are detrital transport of benthic bioclasts from the Bay of Biscay continental shelf, supplemented by hemipelagic carbonates from plankton, including coccolithophores and planktonic foraminifera. Analysis of a sediment trap deployed in Guilvinec Canyon showed extensive transport of shelf sediments down the canyon associated with tidal pumping, and possibly with storm events (Kriphounoff et al., 2014). Coastal environments of the Bay of Biscay host abundant maerl beds (calcareous algae, composed of high-Mg calcite), and a variety of molluscs and echinoderms producing aragonite, calcite, and high-Mg calcite skeletons (Ehrhold et al., 2021). Dolomite contributed a consistent 2% to the mineralogical composition of the Guilvinec canyon cores; this is almost certainly detrital, and could come from a wide variety of terrigenous and fluvial sources contributing to sediment delivery to the broad Bay of Biscay shelf (Ehrhold et al., 2021). By contrast, 90% of hemipelagic carbonate production by calcareous phytoplankton is predicted to dissolve before burial in deep-sea sediments (Smith and MacKenzie, 2016).

4.3. Apparent change in sediment & carbonate accumulation rates in cores

4.3.1. Change in accretion rate in core CS01

Core CS01 showed a dramatic increase in coral carbonate production, and mound aggradation rate, in the upper half of the core (above 60 cm, after 685 ybp). This increase could reflect an ecological response to an oceanographic change, or spatial heterogeneity in the growth of the coral thicket.

The age of the period of increased coral carbonate accumulation and reef accretion in core CS01 corresponds roughly to the end of the Medieval warm period (MWP) and the start of the Little Ice Age (LIA). The Bay of Biscay is quite central between the Holocene northeast Atlantic coral province and the Pleistocene and Younger Dryas eastern Atlantic coral province, stretching from Northwest Africa to the Gulf of Cadiz Frank, 2011). An increase in coral growth with a slightly colder climate would be consistent with small-scale changes in Mediterranean Outflow Water production recorded in Neodymium isotopes in coral skeletons (Montero-Serrano et al., 2013), and with enhanced Mediterranean vertical circulation during late glacial stadials (Toucanne et al., 2012). Holocene cold-water coral reef accretion elsewhere in the Northeast Altlantic and Mediterranean has been episodic, with varying rates of accretion, and periods of non-accretion linked to changes in ocean circulation and climate (Douarin et al., 2013; Titschack et al., 2016; Wienberg and Titschack, 2017).

Alternatively, the observed shift in aggradation rate could represent a local facies change on the coral mound. Core CS01 was recovered from the top of a small ridge that is part of a coral mound, although not from the possible mound summit in 750 m water depth (Fig. 2A). Fig. 2B shows extensive areas of apparent sediment waves in Guilvinec Canyon detected in near-bottom ROV-mounted multibeam bathymetry. Core CS02 lies in a flat zone between two slightly steeper zones associated with apparent sediment waves. It is possible that the differences in sediment accumulation rate between cores, and within core CS01 both reflect fine-scale spatial changes in reef growth and sediment accumulation with respect to sediment waves.

With only one core, no definitive conclusions can be reached, and other coring attempts in the Bay of Biscay Holocene reefs during the BobGeo and BobEco campaigns were unsuccessful, although long cores through carbonate mounds were recovered from the Irish Margin (Stapleton et al., 2013). Future research plans include analysis of εNd in corals from core BoBECO CS01, and sortable silt from cores CS01 and CS02 to determine whether there have been changes in water mass and changes in contour current strength through time.

4.3.2. Differences between core CS01 and CS02, and between cores and ROV surveys

Core CS02 showed a consistent rate of sediment accumulation over nearly 5000 years, with almost no change in the (low) abundance of coral rubble. This result is consistent with the goal of core CS02, to sample the sedimentary flank of a coral thicket.

The current rate of coral $CaCO_3$ accumulation based upon the ROV video survey is approximately 1/22 of the rate observed in the upper half of core CS01. Given the very low % live coral cover (2.65 %) observed in Guilvinec Canyon, a 22x increase in carbonate production would imply 55% live coral cover, all other things being equal. This cover value is far higher than observed on reefs anywhere in the Bay of Biscay (van den Beld et al., 2017), but is not unusual on healthy reefs on the Norwegian shelf (Lindberg and Mienert, 2005; Davies, 2017), or parts of the Mediterranean (Wienberg and Titschack, 2017).

The apparent difference in the % live coral cover observed in the ROV surveys and the core CS01 may reflect a combination of anthropogenic factors relating to trawling and sediment mobilization, and seawater warming, and decreased Mediterranean Overflow Water production since the Industrial Revolution and the end of the Little Ice Age (Montero-Serrano et al., 2013).

4.4. Regional differences in carbonate accumulation rates

Reported calcium carbonate accumulation rates in core from cold-water coral reef ecosystems elsewhere in the NE Atlantic and Mediterranean (Titschack et al. 2015, 2016; Wienberg and Titschack, 2017) are

up to one order of magnitude higher than those reported from the Bay of Biscay. This difference may relate to higher coral abundance, or to higher coral growth and sediment accumulation rates in those regions, than in the Bay of Biscay, or perhaps to the fact that core CS01 was not recovered from the summit of a coral mound, where highest growth is expected (Wienberg and Titschack, 2017).

Nonetheless, carbonate accumulation rates in the Bay of Biscay cold-water coral thickets are quite low relative to other cold-water coral provinces, and especially compared to other cold-water carbonate depositional environments such as calcareous algae (maerl), where photosynthesis provides an additional energy source (Wisshak et al., 2019; Teed et al., 2020).

Globally, cold-water coral reefs are recognized as locally important, but globally small, contributors to cold-water carbonate sediment production (James, 1997; James and Lukasik, 2010; Smith and MacKenzie, 2016). Nonetheless, the ability of cold-water coral reefs to trap and bury carbonates, thus adding them to the sedimentary record, rather than the pool of dissolved carbonate in the ocean, makes them important local contributors to the global carbonate cycle.

5. Conclusions

Calcium carbonate production in deep-sea coral thickets of Guilvinec Canyon, Bay of Biscay, was measured using an adaptation of the Reef-Budget methodology from tropical coral reefs to deep-sea coral systems.

Recent coral carbonate production in Guilvinec Canyon was very low, less than 7 g $CaCO_3$ m^{-2} y^{-1}, reflecting average live coral cover values less than 3%.

Coral calcium carbonate accumulation in a sediment core averaged 70 g m^{-2} y^{-1} over the last ~2 ky, with maximum values of 148 g coral $CaCO_3$ m-2 y^{-1} observed in the upper 60 cm of a piston core through a reef mound. Changes in carbonate accumulation rate through the past 2000 y may reflect changes in oceanographic condition, local habitat heterogeneity, or a combination of these.

Much higher rates of coral carbonate accumulation in the sediment core than on the extant coral thickets may reflect a combination of time-averaging, sediment compaction, and recent decline in coral condition. Modern threats to Bay of Biscay corals include direct damage from bottom-contact fishing, increased sediment flux down submarine canyons related to extensive bottom trawling on the Bay of Biscay Shelf, increased bottom water temperatures, and declining bottom water carbonate saturation.

CRediT authorship contribution statement

Evan Edinger: Writing – original draft, Visualization, Methodology, Investigation, Funding acquisition, Formal analysis, Data curation, Conceptualization. **Jean-François Bourillet:** Writing – review & editing, Writing – original draft, Visualization, Resources, Project administration, Methodology, Investigation, Funding acquisition, Data curation, Conceptualization. **Lenaïck Menot:** Writing – review & editing, Resources, Methodology, Investigation, Funding acquisition, Data curation. **Franck Lartaud:** Writing – review & editing, Supervision, Resources, Formal analysis. **Mathilde Chemel:** Writing – review & editing, Investigation, Data curation. **Stephan Jorry:** Writing – review & editing, Supervision, Resources, Project administration, Methodology, Funding acquisition, Formal analysis.

Declaration of competing interest

The authors declare that they have no known competing financial interests or personal relationships that could have appeared to influence the work reported in this paper.

Acknowledgements

We thank the crew and officers of *N/O Pourquoi Pas?* for their contributions to the successful acquisition of data and samples. We thank Inge van den Beld for making images and analysis data available. Norbert Frank contributed U-Th ages of coral samples from core CS01. Sylvain Bermell assisted with GIS analyses and merging datasets, and Jérémie Gouriou with XCT measurements. We thank Samuel Toucanne, Aurélie Penaud, and Axel Ehrhold for discussions, particularly with respect to Bay of Biscay regional sedimentology and oceanography & paleoceanography. Max Wisshak and one anonymous reviewer provided useful suggestions to improve the manuscript. Field work was supported by EC FP7 project CoralFISH under grant agreement no. 213144. Subsequent analyses were supported by IFREMER, NSERC Discovery Grant RPGIN-2020-04183 to EE, and by Memorial University sabbatical research grants to EE. Dedicated to the memory of Iris Edinger.

Appendix A. Supplementary data

Supplementary data to this article can be found online at https://doi.org/10.1016/j.dsr2.2024.105451.

Data availability

Data will be made available on request.

References

Arnaud-Haond, S., Grehan, A., 2011a. BOBECO LEG1 cruise, RV Pourquoi pas. https://doi.org/10.17600/11030090.

Arnaud-Haond, S., Grehan, A., 2011b. BOBECO LEG2 cruise, RV Pourquoi pas. https://doi.org/10.17600/11030180.

Arnaud-Haond, S., Moalic, Y., 2011. Compte Rendu de Campagne à la Mer BobEco. IFREMER Centre Bretagne, France, p. 119p.

Arnaud-Haond, S., Van den Beld, I.M.J., Becheler, R., Orejas, C., Menot, L., Frank, N., Grehan, A., Bourillet, J.-F., 2017. Two pillars of cold-water coral reefs along Atlantic European margins: prevalent association of Madrepora oculata with Lophelia pertusa, from reef to colony scale. Deep-Sea Research II 145, 110–119.

Beuck, L., Freiwald, A., 2005. Bioerosion patterns in a deep-water Lophelia pertusa (scleractinia) thicket (propeller mound, northern porcupine seabight). In: Freiwald, Roberts (Eds.), Cold-water Corals and Ecosystems. Springer-Verlag, Berlin, pp. 915–936, 2005.

Bøe, R., Bellec, V.K., Dolan, M.F., Buhl-Mortensen, P., Rise, L., Buhl-Mortensen, L., 2016. Cold-water coral reefs in the Hola glacial trough off Vesteralen, Northern Norway. In: Dowdeswell, et al., 2016, Atlas of Submarine Glacial Landforms: Modern, Quaternary and Ancient. Geol. Soc. Lond. Memoirs 46, 309–310.

Boerboom, C.M., Smith, J.E., Risk, M.J., 1998. Bioerosion and micritization in the deep-sea coral Desmophyllum cristagalli. Hist. Biol. 13, 53–60. https://doi.org/10.1080/08912969809386572.

Bosschler, H., Meesters, E.H., 1993. Depth-related changes in the growth rate of Montastrea annularis. Proc. 7th Int. Coral Reef Symp 1, 507–512.

Bourillet, J.-F., Zaragozi, S., Mulder, T., 2006. The French Atlantic margin and the deep sea submarine systems. Geo Mar. Lett. 26, 311–315. https://doi.org/10.1007/s00367-006-0042-2.

Bourillet, J.-F., Damy, G., Dussud, L., Sultan, N., Woerther, P., Migeon, S., 2007. Behaviour of a piston corer from accelerometers and new insights on quality of the recovery. Proc. 6th Intern. Offshore Site Investigation and Geotechnics Conference: Confronting New Challenges and Sharing Knowledge, pp. 57–62.

Bourillet, J.-F., 2009. BOBGEO cruise report, RV Pourquoi pas. https://doi.org/10.17600/9030060.

Bourillet, J.-F., 2010. BOBGEO2 cruise report, RV Le Suroît. https://doi.org/10.17600/10020020.

Bourillet, J.-F., de Chambure, L., Loubrieu, B., 2012. Sur les traces des coraux d'eau froide du Golfe de Gascogne: 8 cartes bathymorphologiques et géomorphologiques au 1/100,000. Editions Quae, Paris.

Bourillet, J-F., Veslin, M., Pertuisot, C., 2013. Mission Bob-Eco- Rapport Carottage, correction to Arnaud-Haond & Grehan, 2011, Bob-Eco cruise report, correction 24 April 2013, 43 p.

Brooke, S., Young, C.M., 2009. In-situ measurement of survival and growth of Lophelia pertusa in the northern Gulf of Mexico. Mar. Ecol. Progr. Ser. 397, 153–161.

Büscher, J., Form, A.U., Riebesell, U., 2017. Interactive effects of ocean acidification and warming on growth, fitness and survival of the cold-water coral Lophelia pertusa under different food availabilities. Front. Mar. Sci. 4, 101. https://doi.org/10.3389/fmars.2017.00101.

Büscher, J.V., Wisshak, M., Form, A.U., Titschack, J., Nachtigall, K., Riebesell, U., 2019. In-situ growth and bioerosion rates of Lophelia pertusa in a Norwegian Fjord and

open shelf cold-water coral habitat. PeerJ 7, e7586. https://doi.org/10.7717/pperJ.7586.
Büscher, J.V., Form, A.U., Wisshak, M., Kiko, R., Riebesell, U., 2022. Cold-water coral ecosystems under future ocean change: live coral performance vs. Framework dissolution and bioerosion. Limnol. Oceanogr. 67, 2497–2515. https://doi.org/10.1002/lno.12217.
Chapron, L., Le Bris, N., Durrieu de Madron, X., Peru, E., Galand, P.E., Lartaud, F., 2020. Long-term monitoring of cold-water coral growth shows response to episodic meteorological events in the NW Mediterranean. Deep-Sea Res. I 160, 103255. https://doi.org/10.1016/j.dsr.2020.103255.
Chapron, L., Galand, P.E., Pruski, A.M., Vetion, G., Robin, S., Lartaud, F., 2021. Resilience of cold-water coral holobionts to thermal stress. Proc. R. Soc. A B 288, 20212117. https://doi.org/10.1098/rspb.2021.2117.
Chemel, M., 2023. Effect of Temperature on Cold-Water Coral Holobiont in the North-East Atlantic Ocean. Ph.D. thesis, Sorbonne Université, Paris, p. 220.
Chemel, M., Peru, E., Mutlaq Binsarhan, M., Logares, R., Lartaud, F., Galand, P.E., 2024. Cold-water coral mortality under ocean warming is associated with pathogenic bacteria. Environ. Microb. 19 (1), 76. https://doi.org/10.1186/s40793-024-00622-0.
Davies, J.S., 2017. A new classification scheme of European cold-water coral habitats: implications for ecosystem-based management of the deep-sea. Deep-Sea Res. II 145, 102–109. https://doi.org/10.1016/j.dsr2.2017.04.014.
De Mol, L., Van Rooij, D., Pirlet, H., Greinert, J., Frank, N., Quemmerais, F., Henriet, J.-P., 2011. Cold-water coral habitats in the PenMarc'h and Guilvinec Canyons (Bay of Biscay): deep-water versus shallow-water settings. Mar. Geol. 282, 40–52.
Douarin, M., Elliot, M., Nobie, S.R., Sinclair, D., Henry, L.-A., Long, D., Moreton, S.T., Roberts, J.M., 2013. Growth of north-east Atlantic cold-water coral reefs and mounds during the Holocene: a high-resolution U-series and ^{14}C chronology. Earth Plan. Sci. Lett. 375, 176–187. https://doi.org/10.1016/j.epsl.2013.05.023.
Edinger, E.N., Limmon, G.V., Jompa, J., Widjatmoko, W., Heikoop, J.M., Risk, M.J., 2000. Normal coral growth rates on dying reefs: are coral growth rates good indicators of reef health? Mar. Pollut. Bull. 40, 606–617.
Edinger, E.N., Pandolfi, J.M., Kelley, R.A., 2001. Community structure of Quaternary coral reefs compared with Recent life and death assemblages. Paleobiology 27, 669–694.
Edinger, E.N., Burr, G.S., Pandolfi, J.M., Ortiz, J.C., 2007. Age accuracy and resolution of Quaternary corals used as proxies for sea level. Earth Plan. Sci. Lett. 253, 37–49. https://doi.org/10.1016/j.epsl.2006.10.014.
Ehrhold, A., et al., 2021. Fossil maerl beds as coastal indicators of late Holocene paleo-environmental evolution in the Bay of Brest (Western France). Palaeogeogr. Palaeoclim. Palaeoecol. 577, 110525.
Fontela, M., Perez, F.F., Carracedo, L.I., Padin, X.A., Velo, A., Garcia-Ibanez, M.I., L'Herminier, P., 2020. The Northeast Atlantic is running out of excess carbonate in the horizon of cold-water corals communities. Sci. Rep. 10, 14714. https://doi.org/10.1038/s41598-020-7193-2.
Frank, N., and 16 others, 2011. Northeastern Atlantic cold-water coral reefs and climate. Geology 39, 743–746. https://doi.org/10.1130/G31825.1.
Frank, N., Paterne, M., Ayliffe, L.L., van Weering, T., Henriet, J.-P., Blamart, D., 2004. Eastern North Atlantic deep-sea corals: tracing upper intermediate water Δ14C during the Holocene. Earth Plan. Sci. Lett. 219, 297–309. https://doi.org/10.1016/s0012-821X(03)00721-0.
Freiwald, A., 2002. Reef-forming cold-water corals. In: Wefer, et al. (Eds.), Ocean Margin Systems. Springer, pp. 365–385. https://doi.org/10.1007/978-3-662-051.27-6_23.
Freiwald, A., Wilson, J.B., 1998. Taphonomy of modern deep, cold-temperate water coral reefs. Hist. Biol. 1, 37–52. https://doi.org/10.1080/08912969809386571.
Gass, S.E., Roberts, J.M., 2006. The occurrence of the cold-water coral *Lophelia pertusa* (Scleractinia) on oil and gas platforms in the North Sea: colony growth, recruitment and environmental controls on distribution. Mar. Poll. Bull. 52, 549–559.
GEBCO compilation Group, 2021. In: General Bathymetric Chart of the Oceans 2021 grid. https://doi.org/10.5285/c6612cbe-50b3-0cffe053-6c86abc09f8f.
Goslar, T., Czernik, J., Goslar, E., 2004. Low-energy ^{14}C AMS in Poznán radiocarbon laboratory, Poland. Nucl. Instrum. Methods Phys. Res. B 223–224, 5–11.
Guinotte, J.M., Orr, J., Cairns, S., Freiwald, A., Morgan, L., George, R., 2006. Will human-induced changes in seawater chemistry alter the distribution of deep-sea scleractinian corals? Front. Ecol. Environ. 4, 141–146.
Hennige, S.J., Wicks, L.C., Kamenos, N.A., Perna, G., Findlay, H.S., Roberts, J.M., 2015. Hidden impacts of ocean acidification to live and dead coral framework. Proc. R. Soc.B 282, 20150990. https://doi.org/10.1098/rspb.2015.0990.
Hennige, S.J., Wolfram, U., Wickes, L., Murray, F., Roberts, J.M., Kamenos, N.A., Schofield, S., Groetsch, A., Spiesz, E.M., Aubin-Tam, M.-E., Etnoyer, P.J., 2020. Crumbling reefs and cold-water coral habitat loss in a future ocean: evidence of "coralporosis" as an indicator of habitat integrity. Front. Mar. Sci. 7, 668. https://doi.org/10.3389/fmars.2020.00668.
Hubbard, D.K., Miller, A.I., Scaturo, D., 1990. Production and cycling of calcium carbonate in a shelf-edge reef system (St. Croix, US Virgin Islands_: applications to the nature of reef systems in the fossil record. J. Sediment. Petrol. 60, 335–360.
Hubbard, D.K., 1992. Hurricane-induced sediment transport in open-shelf tropical systems – an example from St. Croix, U.S. Virgin Islands. J. Sediment. Petrol. 62, 946–960.
James, N.P., 1997. In: The cool-water carbonate depositional realm. In James et al., vol. 56. SEPM Special Publication, pp. 1–20. https://doi.org/10.2110/pec.97.56.0001.
James, N.P., Lukasik, J., 2010. Cool-and cold-water neritic carbonates. Facies Models 4. Geological Association of Canada, pp. 371–399.
Jorry, S.J., Jouet, G., Edinger, E., Toucanne, S., Counts, J.W., Miramontes, E., Courgeon, S., Vasquez-Reveiros, N., Le Roy, P., Camoin, G.F., 2020. From platform top to adjacent deep sea: new source-to-sink insights into carbonate sediment production and transfer in the SW Indian Ocean (Glorieuses archipelago). Mar. Geol. 423, 106144. https://doi.org/10.1016/j.margeo.2020.106144.
Joubin, M.L., 1922. In: Les Coraux de mer Profonde Nuisibles aux Chalutiers. Office scientifique et technique des peches maritimes, notes et memoires No. 18, Editions Blondel La Rougery, Paris.
Kowalewski, M., 1996. Time-averaging, overcompleteness, and the geological record. J. Geol. 104, 317–326.
Kriphounoff, A., Caprais, J.-C., Le Bruchec, J., Rodier, P., Noel, P., Cathalot, C., 2014. Deep cold-water coral ecosystems in the Brittany submarine canyons (Northeast Atlantic): hydrodynamics, particle supply, respiration, and carbon cycling. Limnol. Oceanogr. 59, 87–98.
Larcom, E.A., McKean, D.L., Brooks, J.M., Fisher, C.R., 2014. Growth rates, densities, and distribution of *Lophelia pertusa* on artificial structures in the Gulf of Mexico. Deep-Sea Res. I 85, 101–109. https://doi.org/10.1016/j.dsr.2013.12.005.
Larsson, A.I., Lundalv, T., van Oevelen, D., 2013. Skeletal growth, respiration rate and fatty acid composition in the cold-water coral Lophelia pertusa under varying food conditions. Mar. Ecol. Prog. Ser. 483, 169–184. https://doi.org/10.3354/meps10284.
Lartaud, F., Pareige, S., de Rafelis, M., Feuillassier, L., Bideau, M., Peru, E., De la Vega, E., Nedoncelle, K., Romans, P., Le Bris, N., 2014. Temporal changes in the growth of two Mediterranean cold-water coral species, in situ and in aquaria. Deep Sea Res. Part II Top. Stud. Oceanogr. 99, 64–70. https://doi.org/10.1016/j.dsr2.2013.06.024.
Lartaud, F., Meistertzheim, A.L., Peru, E., Le Bris, N., 2017. *In situ* growth experiments of reef-building cold-water corals: the good, the bad and the ugly. Deep Sea Res. Oceanogr. Res. Pap. 121, 70–78. https://doi.org/10.1016/j.dsr.2017.01.004.
Lartaud, F., Mouchi, V., Chapron, L., Meistertzheim, A.-L., Le Bris, N., 2019. Growth Patterns of Mediterranean Calcifying Cold-Water Corals. in: Past, Present and Future of Mediterranean Cold-Water Corals, vol. 9. Springer "Coral Reefs of the World, pp. 405–422. https://doi.org/10.1007/978-3-319-91608-8_36.
Le Danois, E., 1948. Les profondeurs de la mer: trente ans de recherches sur la faune sous-marine au large des cotes de France. Payot, Paris, pp. 303–p.
Lindberg, B., Mienert, J., 2005. Postglacial carbonate production by cold-water corals on the Norwegian shelf and their role in global carbonate budget. Geology 33, 537–540. https://doi.org/10.1330/G21577.1.
Mengual, B., Cayocca, F., Le Hir, P., Draye, R., Laffargue, P., Vincent, B., Garlan, T., 2016. Influence of bottom trawling on sediment resuspension in the 'Grande-Vasiere' area (Bay of Biscay, France). Ocean Dynam. 66, 1181–1207. https://doi.org/10.1007/s10236-016-0974-7.
Mengual, B., Le Hir, P., Cayocca, F., Garlan, T., 2019. Bottom trawling contribution to the spatio-temporal variability of sediment fluxes on the continental shelf of the Bay of Biscay (France). Mar. Geol. 414, 77–91. https://doi.org/10.1016/j.margeo.2019.05.009.
Menot, L., 23 others, 2023. CheReef: a multi-disciplinary and multi-scale project to assess and predict thehealth of deep-sea corals in the Bay of Biscay (NE Atlantic). In: 8th International Symposium on Deep-Sea Corals, pp. 163–164, 29 May – 2 June, 2023, program and abstracts.
Montero-Serrano, J.-C., Frank, N., Tisnerat-Laborde, N., Colin, C., Wu, C.-C., Shen, C.-C., Copard, K., Orejas, C., Gori, A., De Mol, L., Van Rooij, D., Reverdin, G., Douville, E., 2013. Decadal changes in the mid-depth water mass dynamic of the Northeastern Atlantic margin (Bay of Biscay). Earth Plan. Sci. Lett. 364, 134–144. https://doi.org/10.1016/j.epsl.2013.01.012.
Morato, T., 58 others, 2020. Climate-induced changes in the suitable habitat of cold-water corals and commercially important deep-sea fishes in the North Atlantic. Glob. Change Biol. 26, 2181–2202.
Odum, H.T., Odum, E.P., 1955. Trophic structure and productivity of a windward coral reef community on Eniwetok Atoll. Ecol. Monogr. 25, 291–320.
Orejas, C., Ferrier-Pagès, C., Reynaud, S., Tsounis, G., Allemand, D., Gili, J.M., 2011. Experimental comparison of skeletal growth rates in the cold-water coral *Madrepora oculata* Linnaeus, 1758 and three tropical scleractinian corals. J. Exp. Mar. Biol. Ecol. 405, 1–5. https://doi.org/10.1016/j.jembe.2011.05.008.
Orejas, C., Jimenez, C., 2017. The builders of the oceans – Part I: coral architecture from the tropics to the poles, form the shallow to the deep. In: Rossi, et al. (Eds.), Marine Animal Forests. Springer, pp. 627–655. https://doi.org/10.1007/978-3-319-21012-4_10.
Perry, C.T., Spencer, T., Kench, P., 2008. Carbonate budgets and reef production states: a geomorphic perspective on the ecological phase-shift concept. Coral Reefs 27, 853–866.
Pandolfi, J.M., and 11 others, 2006. Mass mortality following disturbance in Holocene coral reefs from Papua New Guinea. Geology 34, 949–952. https://doi.org/10.1330/G22814A.
Penaud, A., and 13 others, 2020. Oceanic versus continental influences over the last 7 kyrs from a mid-shelf record in the northern Bay of Biscay (NE Atlantic). Quat. Sci. Rev. 229, 106135. https://doi.org/10.1016/j.quascirev.2019.106135.
Perry, C.T., and 26 others, 2018. Loss of coral reef growth capacity to track future increases in sea level. Nature 558, 396–400. https://doi.org/10.1038/s41586-018-0194-z.
Perry, C.T., Edinger, E.N., Kench, P.S., Murphy, G.N., Smithers, S.G., Steneck, R.S., Mumby, P.J., 2012. Estimating rates of biologically driven coral reef framework production and erosion: a new census-based carbonate budget methodology and applications to the reefs of Bonaire. Coral Reefs 31, 853–868. https://doi.org/10.1007/S00338-012-0901-4.
Perry, C.T., Murphy, G.N., Kench, P.S., Smithers, S.G., Edinger, E.N., Steneck, R.S., Mumby, P.J., 2013. Caribbean-wide decline in carbonate production threatens coral reef growth. Nat. Commun. 4, 1402. https://doi.org/10.1038/ncomms2409.

Perry, C.T., Murphy, G.N., Kench, P.S., Edinger, E.N., Smithers, S.G., Steneck, R.S., Mumby, P.J., 2014. Changing dynamics of Caribbean reef carbonate budgets: emergence of reef bioeroders as critical controls on present and future reef growth potential. Proc. R. Soc. B 281, 2018. https://doi.org/10.1098/rspb.2014.2018.

Perry, C.T., Murphy, G.N., Graham, N.A.J., Wilson, S.K., Januchowski-Hartley, F.A., East, H.K., 2015. Remote coral reefs can sustain high growth potential and may match future sea level trends. Sci. Rep. 5, 18289. https://doi.org/10.1038/srep18289.

Reimer, P.J., 29 others, 2013. IntCal13 and Marine13 radiocarbon age calibration curves 0–50,000 Years cal BP. Radiocarbon 55 (4), 1869–1887.

Roberts, J.M., Wheeler, A., Freiwald, A., Cairns, S., 2009. Cold-water Corals: the Biology and Geology of Deep-Sea Coral Habitats. Cambridge University Press, p. 334. https://doi.org/10.1017/CBO9780511581588.

Schönberg, C., Fang, J.K.H., Carreiro-Silva, M., Tribollet, A., Wisshak, M., 2017. Bioerosion: the other ocean acidification problem. ICES J. Mar. Sci. 74, 895–925. https://doi.org/10.1093/icesjms/fsw254.

Scoffin, T., Stearn, C., Boucher, D., Frydl, P., Hawkins, C.M., Hunter, I.G., MacGeachy, J. K., 1980. Calcium carbonate budget of a fringing reef on the west coast of Barbados. I. Erosion, sediments and internal structure. Bull. Mar. Sci. 30, 475–508.

Scoffin, T.P., 1993. The geological effects of hurricanes on coral reefs and the interpretation of storm deposits. Coral Reefs 12, 203–221.

Smith, S.V., MacKenzie, F.T., 2016. The role of $CaCO_3$ reactions in the contemporary oceanic CO_2 cycle. Aquat. Geochem. 22, 153–175. https://doi.org/10.1007/s10498-015-9282-y.

Stapleton, F., Murray, J., Grehan, A., Duffy, G., Williams, M., 2013. 2013. A geological and geophysical description of the Arc Mounds, southwest Porcupine Bank. NUI Galway, INFOMAR final Report 104. https://maps.marine.ie/infomarData/researchmap/reports/2011/INF-11-30-MUR.pdf.

Stearn, C.W., Scoffin, T.P., Martindale, W., 1977. Calcium carbonate budget of a fringing reef on the West Coast of Barbados. Part 1—zonation and productivity. Bull. Mar. Sci. 27, 479–510.

Sweetman, A., 21 others, 2017. Major impacts of climate change on deep-sea benthic ecosystems. Elem. Sci. Ath. 5, 4.

Teed, L., Belanger, D., Gagnon, P., Edinger, E., 2020. Calcium carbonate ($CaCO_3$) production of a subpolar rhodolith bed: methods of estimation, effect of bioturbators, and global comparisons. Estuar. Coast Shelf Sci. 242, 106822. https://doi.org/10.1016/j.ecss.2020.106822.

Titschack, J., Baum, D., De Pol Holz, R., Lop_ez Correa, M., Forster, N., Flögel, S., Hebbeln, D., Freiwald, A., 2015. Aggradation and carbonate accumulation of Holocene Norwegian cold-water coral reefs. Sedimentology 62, 1873–1898.

Titschack, J., Fink, H.G., Bau, D., Wienberg, C., Hebbeln, D., Freiwald, A., 2016. Mediterranean cold-water corals – an important regional carbonate factory? The Depositional Record 2, 74–96.

Tomašových, A., Dominici, S., Nawrot, R., Zuschin, M., 2023. Temporal scales, sampling designs, and age distributions in marine conservation paleobiology. In: Nawrot, et al. (Eds.), Conservation Paleobiology of Marine Ecosystems, vol. 529. Geol. Soc. Lond. Spec. Pub. https://doi.org/10.1144/SP529-2022-361

Toucanne, S., Zaragosi, S., Bourillet, J.-F., Gibbard, P.L., Eynaud, F., Giraudeau, J., Turon, J.-L., Cremer, M., Cortijo, E., Martinez, P., Rossignol, L., 2009. A 1.2 Ma record of glaciation and fluvial discharge from the West European Atlantic margin. Quat. Sci. Rev. 28 (25–26), 2974–2981. https://doi.org/10.1016/j.quascirev.2009.08.003.

Toucanne, S., Jouet, G., Ducassou, E., Bassetti, M.-A., Dennielou, B., Minto'o, C.M.A., Lahmi, M., Touyet, N., Charlier, K., Lericolais, G., Mulder, T., 2012. A 130,000 year record of levantine intermediate water flow variability in the corsica trough, Mediterranean Sea. Quat. Sci. Rev. 33, 55–73. https://doi.org/10.1016/j.quascirev.2011.11.020.

van den Beld, I., Guillaumont, B., Menot, L., Christophe, B., Arnaud-Haond, S., Bourillet, J.-F., 2017a. Marine litter in submarine canyons of the Bay of Biscay. Deep Sea Res. II 145, 142–152.

van den Beld, I., Bourillet, J.-F., Arnaud-Haond, S., de Chambure, L., Davies, J.S., Guillaumont, B., Olu, K., Menot, L., 2017b. Cold-water coral habitats in submarine canyons of the Bay of Biscay. Front. Mar. Sci. 4, 118. https://doi.org/10.3389/fmars.2017.00118.

van der Kaaden, A.-S., Mohn, C., Gerkema, T., Maier, S.R., de Froe, E., van de Koppel, J., Rietkerkm, M., Soetaert, K., van Ouvelen, D., 2021. Feedbacks between hydrodynamics and cold-water coral mound development. Deep-Sea Res. I 178, 103641, 0.1016/j.dsr.2021.103641.

Van Rooij, D., De Mol, L., Le Guilloux, E., Wisshak, M., Huvenne, V.A.I., Mouremans, R., Henriet, J.-P., 2010. Environmental setting of deep-water oysters in the Bay of Biscay. Deep-Sea Res. I 57, 1561–1572.

Wienberg, C., Titschack, J., 2017. Framework-building scleractinain cold-water corals through space and time: a late Quaternary North Atlantic perspective. In: Rossi, S., et al. (Eds.), Marine Animal Forests. Springer, pp. 699–732. https://doi.org/10.1007/978-3-319-21012-4_16.

Wisshak, M., Form, A., Jakobsen, J., Freiwald, A., 2010. Temperate carbonate cycling and water mass properties from intertidal to bathyal depths (Azores). Biogeosciences 7, 2379–2396.

Wisshak, M., Tribollet, A., Golubic, S., Jakobsen, J., Freiwald, A., 2011. Temperate bioerosion: ichnodiversity and biodiversity from intertidal to bathyal depths (Azores). Geobiology 9, 492–520. https://doi.org/10.1111/j.1472-4669.2011.00299.x.

Wisshak, M., Schönberg, C.H.L., Form, A., Freiwald, A., 2012. Ocean acidification accelerates reef bioerosion. PLoS One 7 (9), e45124. https://doi.org/10.1371/journal.pone.0045124.

Wisshak, M., Schönberg, C.H.L., Form, A., Freiwald, A., 2014. Sponge bioerosion accelerated by ocean acidification across species and latitudes? Helgol. Mar. Res. 68, 253–262. https://doi.org/10.1007/s10152-014-0385-4.

Wisshak, M., Berning, B., Jakobsen, J., Freiwald, A., 2015. Temperate carbonate production: biodiversity of calcareous epiliths from intertidal to bathyal depths (Azaores). Mar. Biodiv. 45, 87–112.

Wisshak, M., Neumann, H., Rüggeberg, A., Büscher, J.V., Linke, P., Raddatz, J., 2019. Epibenthos dynamics and environmental fluctuations in two contrasting polar carbonate factories (mosselbukta and bjørnøy-banken, svalbard). Front. Mar. Sci. 6, 667. https://doi.org/10.3389/fmars.2019.00667.

Wisshak, M., Meyer, N., Kuklinski, P., Ruggeberg, A., Freiwald, A., 2021. 'Ten years after' – a long-term settlement and bioerosion experiment in an Arctic rhodolith bed (Mosselbukta, Svalbard). Geobiology. https://doi.org/10.1111/gbi.12469.

Zedel, L., and Fowler, W., 2009. Comparison of bondary layer current profiles in locations with and without corals in Haddock Channel, Southwest Grand Banks, p. 97-104, in: Gilkinson, K., Edinger, E., eds., The ecology of deep-sea corals of Newfoundland and Labrador waters: biogeograph, life history, biogeochemistry, and relation to fishes. Can. Tech. Rep. Fish. Aquat. Sci. 2830: 136 p.